Supplementary Information

High-performance n-type organic mixed ionic-electronic conductors enabled by strong cation-π interactions

Zhen Huang[1,2,#], *Peiyun Li*[1,#], *Yuqiu Lei*[3], *Xin-Yu Deng*[1], *Yu-Nan Chen*[2], *Shuangyan Tian*[1], *Xiran Pan*[3], *Xun Lei*[3], *Yuting Zheng*[3], *Jie-Yu Wang*[2], *Ting Lei*[1,*]

[#]These authors contributed equally to this work

*Correspondence and requests for materials should be addressed to T.L. (tinglei@pku.edu.cn).

This file includes:

1. Experimental details
2. Tables S1 to S7
3. Figures S1 to S29
4. Scheme S1
5. Synthetic procedures
6. Spectral Data
7. References

1. Experimental Details

Materials

All chemical reagents were purchased and used as received unless otherwise indicated. All air and water-sensitive reactions were performed under nitrogen atmosphere. Dichloromethane (DCM), tetrahydrofuran (THF), toluene, and *N,N*-dimethylformamide (DMF) were dried by a JC Meyer solvent drying system. Glycol side chains were purchased in Ningbo Boya Poly Advanced Materials Co., LTD.

Chemical Structure and Optoelectronic Property Characterization

^{1}H NMR and ^{13}C NMR spectra were recorded on Bruker ARX-400 (400 MHz), Bruker AVANCE III (500 MHz), and Bruker 600M (600 MHz). All chemical shifts were reported in parts per million (ppm). ^{1}H NMR chemical shifts were referenced to TMS (0.000 ppm) or D_2O (4.800 ppm), ^{13}C NMR chemical shifts were referenced to $CDCl_3$ (77.00 ppm). Mass spectra were recorded on an AB Sciex-5800 MALDI-TOF mass spectrometer or a Bruker Solarix XR mass spectrometer. Elemental analyses were performed on Vario EL elemental analyzer. Thermal gravity analyses (TGA) were carried out on a TA Instrument Q600 SDT analyzer. The Solid-state ^{13}C high-power decoupling with magic angle spinning (HPDec-MAS) NMR were obtained using a 101 MHz WB Solid-State NMR.

Absorption spectra were recorded on PerkinElmer Lambda 750 UV-Vis spectrometer. Cyclic voltammograms were measured through an electrochemical workstation SP-300 (BioLogic Science Instruments). A standard three-electrode setup was established with employing polymer-coated ITO glass slides (or a glassy carbon electrode) as the working electrode (WE), a block of platinum mesh as the counter electrode (CE), and an Ag/AgCl as the reference electrode (RE), further calibrated against ferrocene (Fc/Fc^+). The measurements were carried out in aqueous solution with 0.1 M NaCl or in acetonitrile with 0.1 M tetrabutylammonium hexafluorophosphate as the supporting electrolyte with a scan rate of 50 mV/s. Ionization potentials and electron affinity were obtained using the equation: IP = ($E_{Ox} - E_{Fc/Fc^+} + 4.8$) eV, EA = ($E_{Red} - E_{Fc/Fc^+} + 4.8$) eV.

Theoretical Analysis

Density functional theory (DFT) calculations were performed using Gaussian 16 software package.[1] Geometries and frontier orbitals of the polymers were calculated at B3LYP/6-311g(d,p)

level. The binding energies, TD-DFT calculations (n states = 100), restrained electrostatic potential and conformation analysis were calculated at ωB97XD/6-311g(d,p) level. Non-covalent interaction (NCI) analysis and Mayer bond analysis are based on the interaction region indicator (IRI) function is performed via the Multiwfn software[2,3] and VMD[4], utilizing the B3LYP/6-31+G(d,p) electron density.

Size exclusion chromatography measurement

Polymer number-average molecular weight (M_n) and molecular weight distributions ($Đ = M_w/M_n$) were measured by size exclusion chromatography (SEC). Hexafluoroisopropanol (HFIPA) SEC analyses were performed on a Waters 1515 instrument equipped with a PLMIXED 7.5×50 mm guard column and two PLMIXED-C 7.5×300 columns and a differential refractive index detector using hexafluoroisopropanol as the eluent at 35 °C with a flow rate of 1 mL min^{-1}. The instrument was calibrated with 10 PMMA standards, and chromatograms were processed with Waters Breeze software.

Electrophoresis analysis

Anion analysis was performed on capillary electrophoresis system (PA800 plus, Beckman, USA), which was equipped with a 60 cm long (50 cm from injection site to detector) fused-silica capillary and a UV detector(230 nm). Relavent reagents were available in the anion analysis kit (A53537, Sciex, USA), and the injection and separation methods were set according to the Instruction Guide. 32 Karat software (Sciex, USA) were applied for data aquisition and peak integration.

AFM and GIWAXS characterization

Atomic force microscopy (AFM) measurements were performed with a Cypher atomic force microscope (Asylum Research, Oxford Instruments). The surface morphology was recorded with a scan rate of 1−2 Hz at the AC mode. Two-dimensional grazing incidence wide-angle X-ray scattering(2D-GIWAXS) measurements were conducted on a Xenocs-SAXS/WAXS system with an X-ray wavelength of 1.5418 Å and 0.2° as an incidence angle. Pilatus 300 K was used as a 2D detector. Data processing was performed in Igor Pro software with Nika and WAXTools packages. Coherences length (L_c) is calculated from the breadth (Δq) of a diffraction peak: $L_c = 0.89 \times 2\pi/\Delta q$.

And paracrystalline disorder (g) is calculated from the center position (q_0) and breadth (Δq) of a diffraction peak: $g = (\Delta q/(2\pi q_0))^{1/2}$.[5,6]

Spectroelectrochemistry

Spectroelectrochemistry was performed with an ITO-coated glass slide, spun cast with the polymer solution (chloroform solution) at a rotating speed of 500 rpm for 45 s without any additional processing. These polymer-coated ITO slides were employed as the WE and immersed into the cuvette filled with 0.1 M aqueous NaCl solution, following with the use of Pt mesh (CE) and Ag/AgCl pellet (RE). A PerkinElmer Lambda 750 UV-vis spectrometer was used with the beam path passing through the electrolyte-filled cuvette and polymer-coated ITO samples. A background spectrum with cuvette/electrolyte/ITO was recorded before a potential was applied to the cell. The potential was applied to the WE for 5 s before the spectra were recorded and lasted for a certain amount of time until the completion of spectrum scanning.

EQCM-D Measurements

EQCM-D measurements were performed using a Q-sense analyzer (QE401, Biolin Scientific). Passive swelling measurements were performed as follows. First, the QCM-D response of bare Au sensors was recorded in air, followed by injection of a 0.1 M NaCl solution into the chamber. The measurements were then stopped when f and D were stable, the sensors were removed, and the polymer layers were spin-casted on the same sensors from solutions in chloroform/chlorobenzene (60:1, v/v). The absolute f value for each polymer-coated sensor was obtained in both air and 0.1 M NaCl after the system was in equilibrium. EQCM-D measurements were performed using an SP-300 (BioLogic Science Instruments) as the voltage source. The three-electrode setup was composed of Ag/AgCl (reference electrode), Pt (counter electrode), and a Au/polymer EQCM-D sensor (working electrode). A voltage bias for 60 s was applied to the working electrode for the measurement of active absorption. Three cycles of cyclic voltammetry were performed for the calculation of ions and water absorption.

Electrochemical impedance spectra

Electrochemical impedance spectra (EIS) were performed on the polymer-coated electrodes using the electrochemical workstation SP-300 (BioLogic Science Instruments). Polymer-coated

electrodes were patterned as squares with different areas through lithography. These polymer-coated electrodes with glass substrate were employed as the working electrode and fully covered with a 0.1 M NaCl solution, followed by the employment of Pt mesh (CE) and Ag/AgCl pellet (RE) to establish a standard three-electrode system. The capacitances of polymers on electrodes with various sizes were obtained through the potentio-EIS method, with setting the DC offset voltage as the maximum achievable doping for each polymer. The AC amplitude of voltage in the form of sine-wave on the WE was set as 10 mV (RMS) and the frequency was scanned from 1 Hz to 100 kHz. The as-obtained Bode plots or Nyquist plots were fitted to an equivalent circuit, namely the Randle's circuit $R_s(R_p||C)$, via the software EC-Lab view. The thickness of the films was determined in the dry state with a DEKTAK profilometer (Bruker).

2. Table S1-S7 and Figure S1-S15

Table S1. Summary of the molecular weights and optoelectronic properties of the polymers.

	M_n[a] (kDa)	M_w[a] (kDa)	PDI[a]	$E_{HOMO,DFT}$[b] (eV)	$E_{LUMO,DFT}$[b] (eV)	$E_{HOMO,CV}$ (eV)	$E_{LUMO,CV}$ (eV)	$E_{g,opt}$[c] (eV)
PANDA	46.4	69.9	1.51	−5.53	−3.96	−5.11	−4.21	1.27
PANDA2	25.1	44.2	1.76	−5.53	−3.96	/	/	/
PNPD	42.5	66.1	1.56	−5.01	−3.07	−4.80	−3.86	1.59

[a]The GPC test was carried out using the HFIP mobile phase. Polymers with ethylene glycol side chains can be disaggregated in HFIP at room temperature.[7] [b]Energy levels of the polymers were calculated using DFT method. Three repeating units are involved in the calculation, and glycol side chains were simplified to methyl groups. The HOMO orbital of PANDA and PANDA2 backbone is the HOMO−6 orbital, for HOMO−5 to HOMO orbital lies on the bromide-lone pair electrons. [c]Optical bandgaps are obtained from the UV-vis-NIR absorption spectra.

Table S2. Comparison of the intermolecular interactions between TDPP and AN/NP.

	Azonia-naphthalene (AN)	Naphthalene (NP)
ΔE_{ass} (kcal mol^{-1})	−22.05	−13.43
ΔE_{ass} (in water) (kcal mol^{-1})	−16.98	−15.09
ΔE_{ass} (in chloroform) (kcal mol^{-1})	−18.80	−15.53

Enthalpy was extracted for thermal analysis as the previous report.[8] The association energy (ΔE_{ass}) is calculated based on the equation, $E_{ass} = E(A+B) - E(A) - E(B) - E_{BSSE}$. Here, $E(A)$ stands for the energy for TDPP moiety, $E(B)$ stands for the energy of AN or NP moiety, E_{BSSE} is an energy correction of orbital overlapping.

We calculate the association energy of TDPP-AN and TDPP-NP in vacuum, water, and chloroform. In all cases, the TDPP-AN complex shows stronger intermolecular interactions than the TDPP-NP complex.

Table S3. Molecular packing data extracted from the 2D-GIWAXS patterns of both polymers.

Direction	q (Å^{-1})	d (Å)	L_C (Å)	g
PANDA (100, lamellar)	0.209	30.1	9.98	0.46
PNPD (100, lamellar)	0.259	24.2	50.8	0.26
PANDA (010, π-π)	1.75	3.59	12.2	0.20
PNPD (010, π-π)	1.72	3.65	15.5	0.18

Table S4. Comparison of the OECT performances for n-type D-A type polymers.

D-A Polymer	τ_{on} (ms)	τ_{off} (ms)	μC^*(F cm^{-1} V^{-1} s^{-1})	$g_{m,norm}$ (S cm^{-1})	V_{th} (V)	Ref.
P(gNDI-gT2)	5	5	NA	0.1085	0.28	9
P(NDI-T2-L2)	40[a]	NA	0.046	0.0084	0.22	10
P90:TBAF(40%)	24	NA	NA	1.5	0.22	11
P90	41	NA	0.0343	0.9	0.25	12
PgNaN	127	NA	0.662	0.212	0.21	13
p(C_4-T2-C_2-EG)	6.2	6[b]	0.01	0.02	0.30	14
p(C_4-T2-C_0-EG)	24.6	12[b]	0.22	0.31	0.32	14
p(C_2-T2)	6.3	1.5[b]	0.20	0.40	0.27	14
p(C_6-T2)	9.6	1[b]	1.29	2.28	0.30	14
2DPP-OD-TEG	500	500	7	1.4	0.8	15
f-BTI2TEG-FT	272	35	15.2	4.60	0.53	16
f-BTI2g-TVTCN	52	17	41.3	12.8	0.68	17
P(gTDPP2FT)	1.75	0.15	54.8	15.3	0.64	18
PANDA	2.43	0.30	40.7	14.7	0.44	This work
PANDA2	1.00	0.18	62.3	19.2	0.47	This work

[a, b]Estimated value from the reported response curve.

Table S5. Summary of the OECT device performance of the two polymers.

	W/L	d (nm)	g_m (mS)	V_{th} (V)	V_g (V)	μC^* (F cm^{-1} V^{-1} s^{-1})	$g_{m,norm}$ (S cm^{-1})
PANDA	10	132	1.94	0.44	0.80	40.7	14.7
	10	152	2.19	0.43	0.80	38.8	14.4
	10	63.0	0.84	0.46	0.80	39.2	13.3
PANDA2	10	30.5	0.490	0.48	0.78	51.8	16.1
	10	30.5	0.590	0.47	0.79	62.3	19.2
	10	30.5	0.410	0.50	0.79	46.3	13.4
PNPD	10	61.4	2.73×10^{-3}	−0.67	−0.84	0.262	4.45×10^{-2}
	10	61.4	2.20×10^{-3}	−0.67	−0.84	0.211	3.59×10^{-2}
	10	61.4	2.46×10^{-3}	−0.67	−0.85	0.223	4.01×10^{-2}

Table S6. Comparison of the stability for some donor-acceptor n-type OECT polymers.

Cycling times (s)	1000	1500	2000	2400	2500	Ref.
PANDA					89%	This work
P(gTDPP2FT)					61%	18
f-BTI2g-TVTCN				75%		17
f-BTI2TEG-FT		80%				16
2DPP-OD-TEG	<80%					15
P(gPzDPP-CT2)			<50%			19
PgNaN			75%			13

Table S7. Comparison of the OECT based inverter gain.

	Gain	V_{DD}	Ref.
PANDA	71	0.5	This work
P(gTDPP2FT)	26.8	0.5	18
2DPP-OD-TEG	50	1.4	15
PNDI2TEG-2Tz	23.4	0.6	20
BBL[a]	55	0.5	21
p(C4-T2-C0-EG)[b]	28	0.8	22

[a]The gain value increases as the V_{DD} increases. BBL has a maximum gain of 100 at 0.7 V, however, a high gain at low voltage is more valuable for further applications. [b]Using vertical geometry.

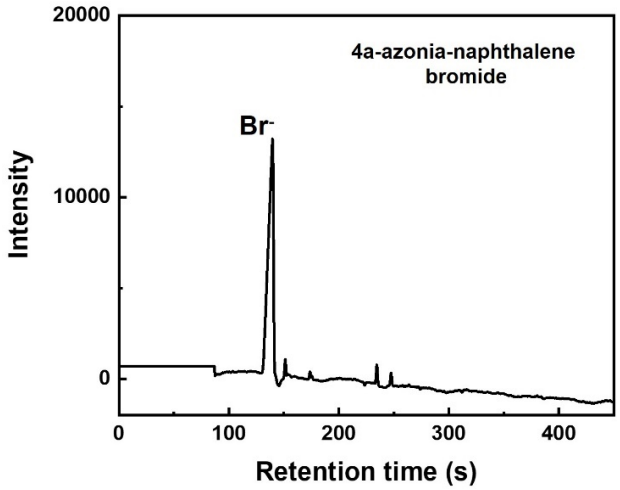

Figure S1. Cataphoretic spectrum of the 4a-azonia-naphthalene bromide. The bromide anion peak dominates 95 % of the total areas of all the peaks, indicating the monomer only contains bromide ion as the counterion.

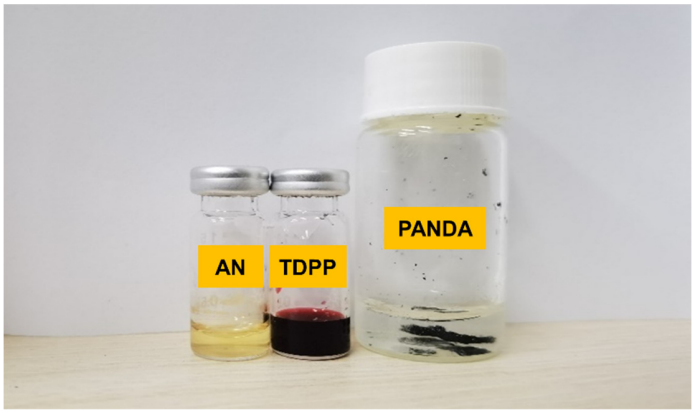

Figure S2. Pictures of azonia-naphthalene (AN) (left), TDPP (middle) and polymer PANDA (right) in water. PANDA is not soluble in water, though its monomers are both soluble, suggesting the strong interactions between AN and TDPP.

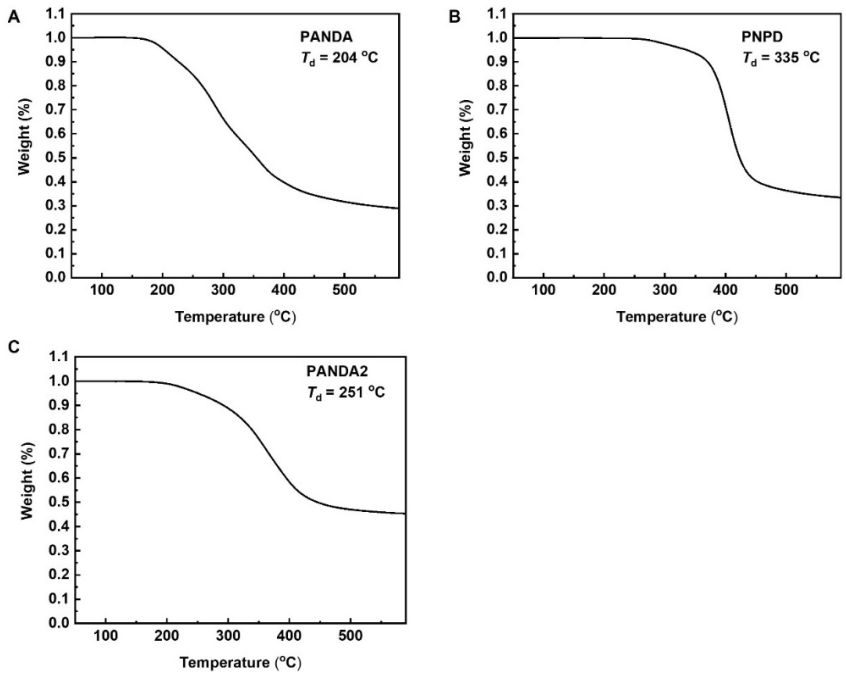

Figure S3. Thermal gravity analyses (TGA) of the polymers. A, PANDA, **B**, PNPD, C PANDA2. The 5 % thermal degradation of PANDA starts from 204 ºC in nitrogen, PANDA starts form 251ºC in nitrogen and PNPD starts from 335 ºC.

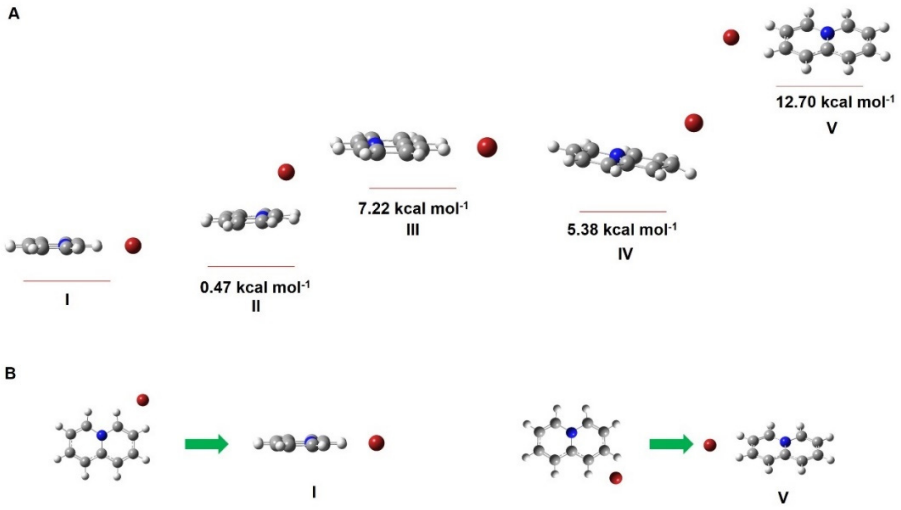

Figure S4. (A) Different optimized structures and their relative energy of AN bromide. Seven initial structures are chosen for optimization. (B) Four initial structures gave two same local minimum structures after optimization. We found that when the bromide ion is close to the hydrogen atoms, the energy is the lowest. When the bromide is close to the nitrogen atom, the

energy is only 0.47 kcal mol^{-1} higher. Therefore, the first two structures are both possible, and we chose the most stable one for representation.

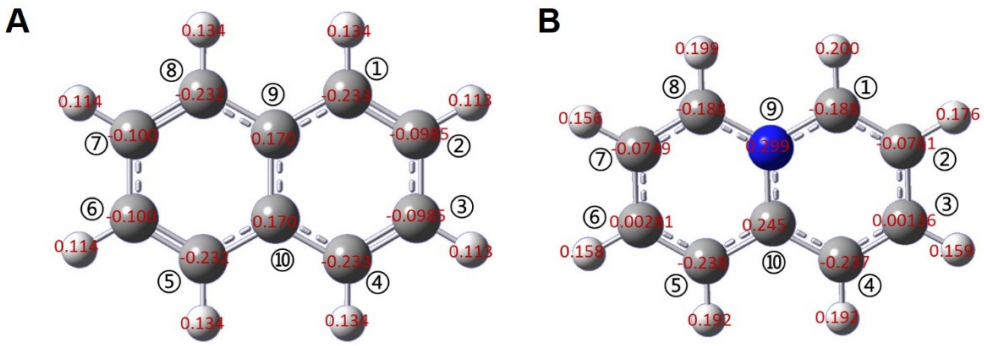

Figure S5. Restrained electrostatic potential (RESP) charge distribution. (A) naphthalene. (B) 4a-azonia naphthalene. Except for the carbon atoms at position 4 and 5, other carbon atoms and all hydrogen atoms have more positive charges after replacing the carbon atom at position 9 with a nitrogen atom, which indicates that the charge is well delocalized on AN and N atom is the most positively charged atom. Thus, we label the positive charge on N to obey conventional molecular structure representation.

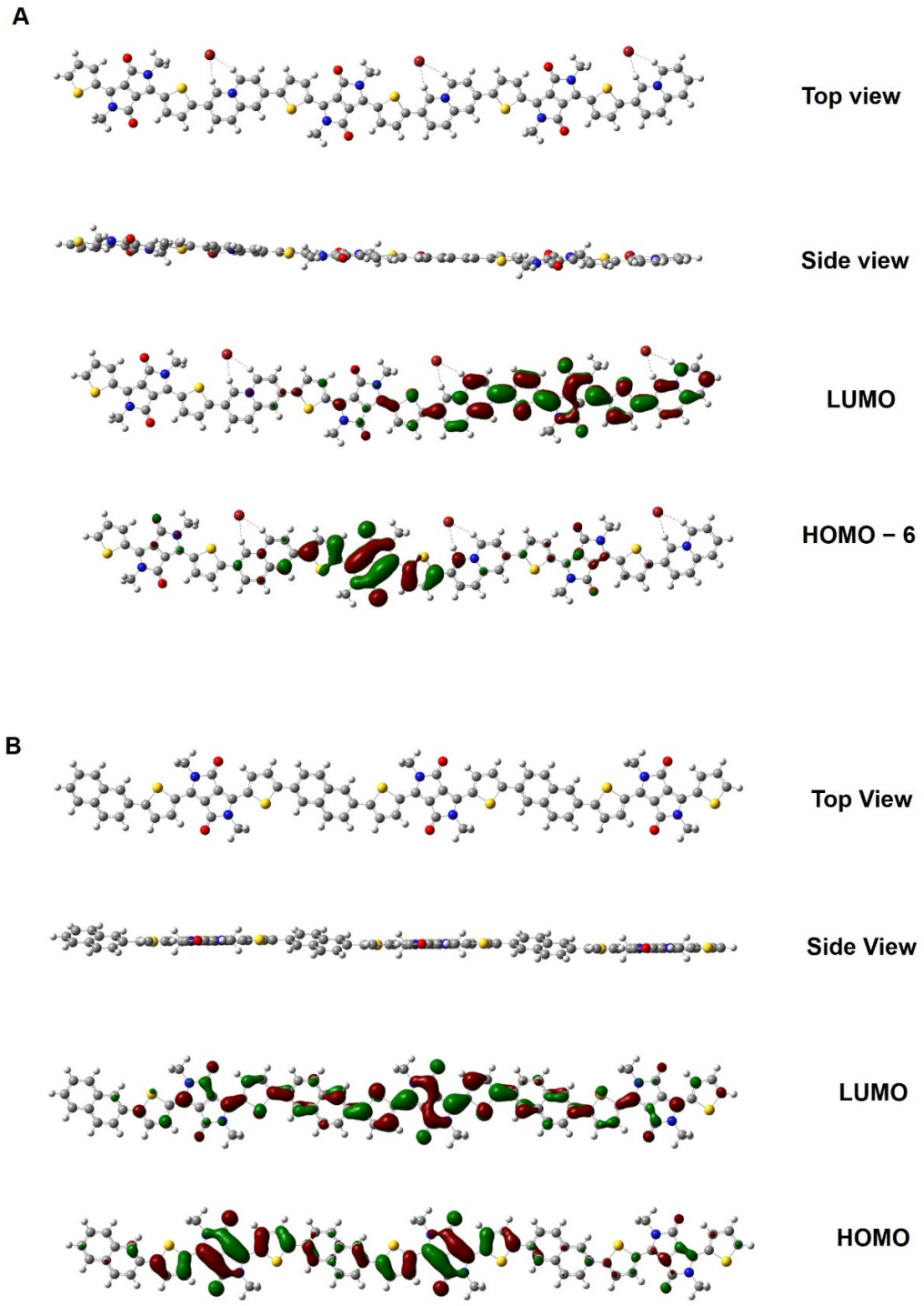

Figure S6. DFT-optimized geometries and molecular frontier orbitals of the trimers of (A), PANDA and (B), PNPD. Glycol side chains were replaced with methyl groups to simplify the calculation. PANDA shows better planarity than PNPD, though they both have a thiophene-benzene single bond connection.

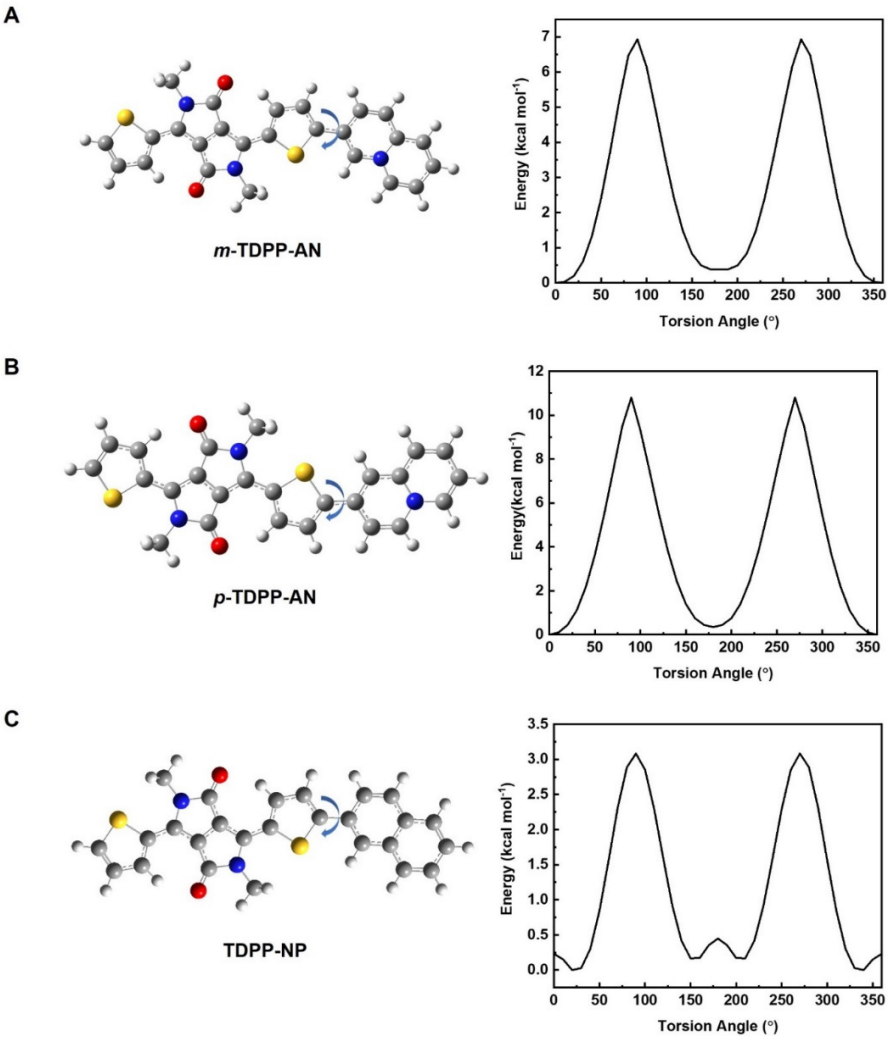

Figure S7. Relaxed potential energy surface (PES) scan of (A) *m*-TDPP-AN, (B) *p*-TDPP-AN, and (C) TDPP-NP unit.

There are two isomers for AN-TDPP connetion, namely, *m*-TDPP-AN and *p*-TDPP-AN. *m*-TDPP-AN: TDPP is at the meta position of the nitrogen atom in AN. *p*-TDPP-AN: TDPP is at the para position of the nitrogen atom in AN. The bond length between thiophene and AN is 1.44 Å (*m*-TDPP-AN) and 1.43 Å (*p*-TDPP-AN), respectively. In contrast, the bond length between naphthalene and TDPP is 1.46 Å when the dihedral angle between the two unit is 23.4°. TDPP-AN connections show a rotational barrier as high as 11 kcal mol^{-1}, which is much higher than other TDPP-neutral building block connections.

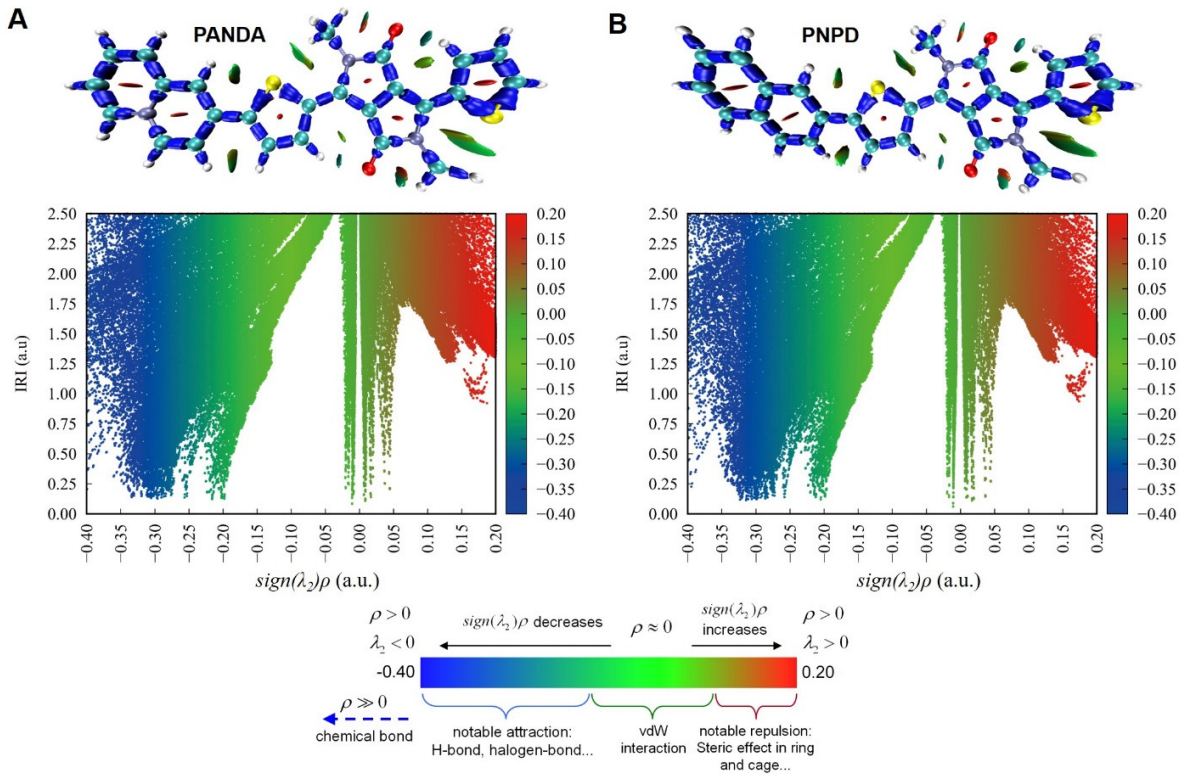

Figure S8. Non-covalent interaction (NCI) analysis of (A) PANDA and (B) PNPD monomer using interaction region indicator (IRI). The top figures show the visualized weak intramolecular interactions and the bottom scatter figures correspond to grid points in 3D space.

To understand the significant difference in relaxed PES scan between PANDA and PNPD, we further explored the steric repulsion, attractive interaction, and donor-accept effects to determine which is the key factor affecting the planarity and rigidity of PANDA. Figure S8 shows the visualization of weak intramolecular interactions. Both molecules exhibit a similar stabilizing hydrogen-sulfur (CH···S) interaction and a hydrogen-hydrogen (H···H) steric repulsion between the aromatic ring and thiophene ring.

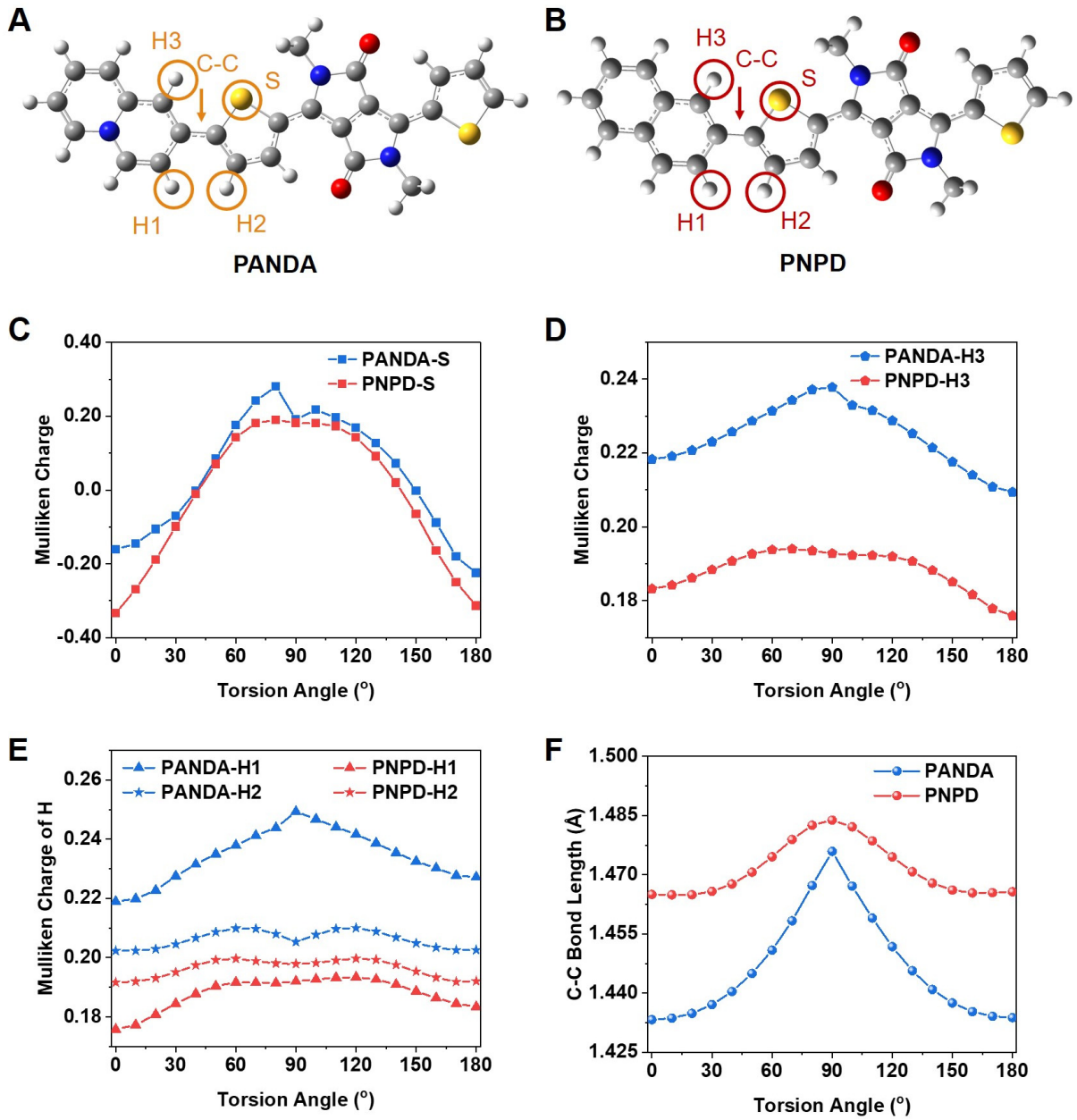

Figure S9. Comparison of the atomic Mulliken charge and bond length as changing the dihedral angles. (A and B), Geometries, atoms, and linkage bond specification of PANDA and PNPD. (C and D), Mulliken atomic charge analysis of S, H1, H2, and H3. **F**, BLA (bond length alternation) of the C-C bond between TDPP and AN/NP.

Regarding the electrostatic mechanism, we analyze the atomic charges on each atom contributing to the non-covalent interactions. Mulliken charges from each of the PES scans were

extracted for the sulfur of thiophene and the hydrogens of adjacent benzene rings (Figure S9, H1-3). These were seen to vary with dihedral angles as the electronic structure of the system changes due to the changes in conjugation and interatomic distances. The partial charges on the sulfur and hydrogens are more positive in PANDA owing to the more electron-deficient nature of the AN and greater intramolecular electron transfer from the thiophene to the AN moiety. The attractive S-H3 interaction could be stronger for PANDA than PNPD due to the more positive charge on H3, while the H1-H2 interaction might be marginally more repulsive. These observations are consistent with the NCI analysis above, i.e., non-covalent interactions are not the main reason for the differences in torsional potential energy scan. Hence, donor-acceptor effects were considered by bond length analysis (BLA) of PANDA and PNPD. As shown in Figure S9F, the length of bridging bond C-C follows closely the change of torsional angle and is minimum at 0°/180°, indicating maximum quinoidal character upon planarization. In contrast, the C-C bond linkage of PANDA exhibits more double bond character than that of PNPD, revealing that the quinoidalization is greatly enhanced by the pronounced push-pull effect in PANDA. This result explains the larger barrier height and higher planarity of PANDA compared to PNPD.

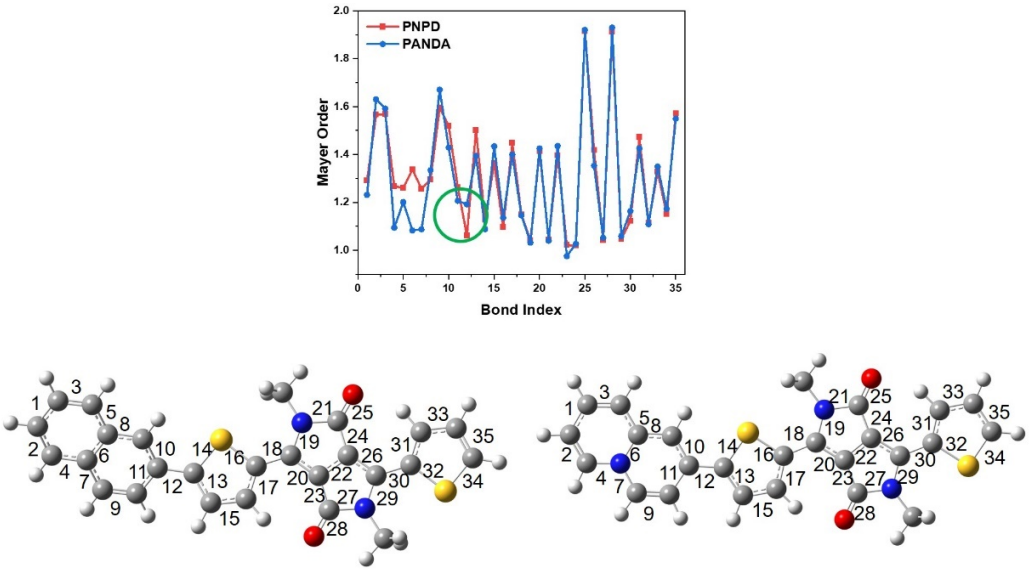

Figure S10. Mayer bond order analysis of the correlating units. Bond 12 was labeled with a green circle, and we can see PANDA has a stronger bond strength for bond 12.

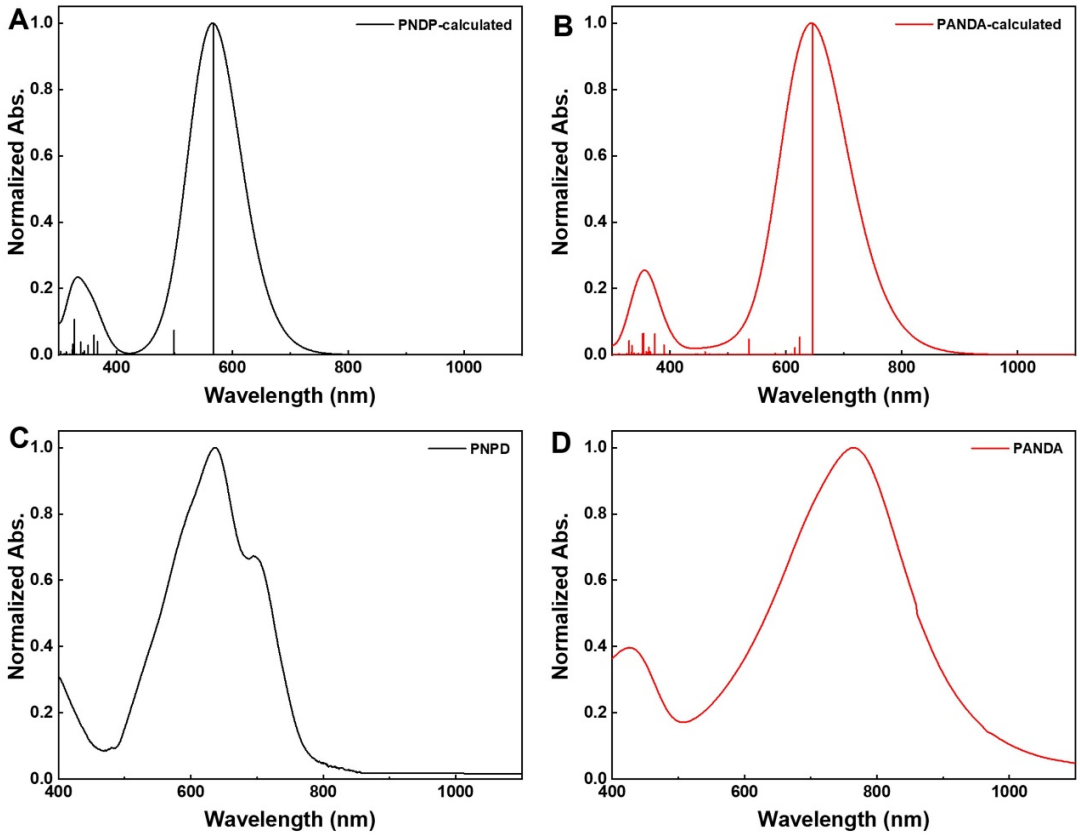

Figure S11 TD-DFT calculated and measured absorption spectra. (A&C) PNPD. (B&D) PANDA. The calculated spectra agree well with the experimental results. The shoulder peak appears in the absorption spectrum of PNPD is due to the polymer aggregation in solution, which has been widely observed in neutral D-A type conjugated polymers.

As shown in the absorption spectra, PNPD has an absorption peak at 636 nm, while PANDA has a peak at 767 nm, redshifted about 130 nm (Figure S20). To better support the UV-vis spectra, we performed time-dependent DFT calculations.[23] The calculated spectra are shown in Figure S20A and S20B. The main peak of PANDA is red-shifted by 80 nm compared to PNPD, which agrees well with our experimental results. We calculated the HOMO/LUMO levels for both polymers, as listed in Table S1. PANDA has a calculated HOMO/LUMO levels of −5.53/−3.96 eV and an electronic band gap of 1.57 eV, and PNPD has a HOMO/LUMO levels of −5.01/−3.07 eV and a gap of 1.94 eV. The calculated energy level values are also consistent with the experimental results. Figure S11 shows that the calculated spectra agree well with the experimental results. The shoulder peak appears in the absorption spectrum of PNPD is due to the polymer

aggregation in solution, which has been widely observed in neutral D-A type conjugated polymers.[24]

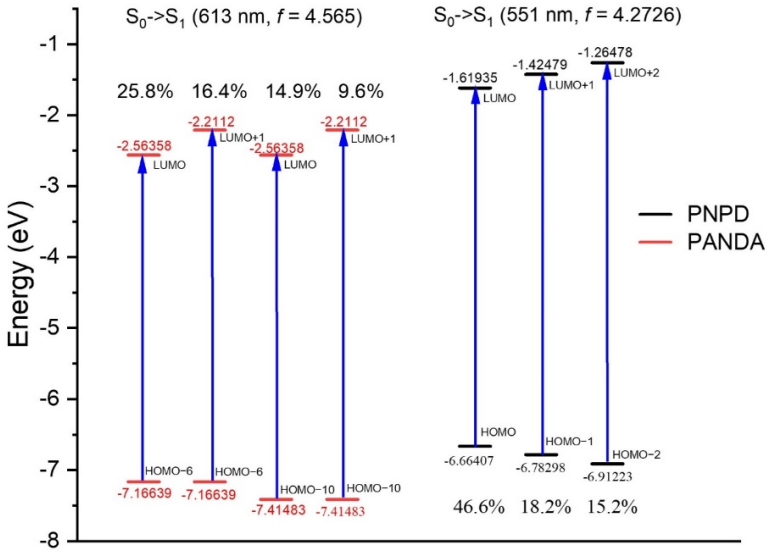

Figure S12. Energy band diagram illustrating the calculated electronic state transitions for PANDA and PNPD.. For each molecule, the wavelength, the oscillator strength (*f*), and the corresponding orbital contribution for the transition are shown.

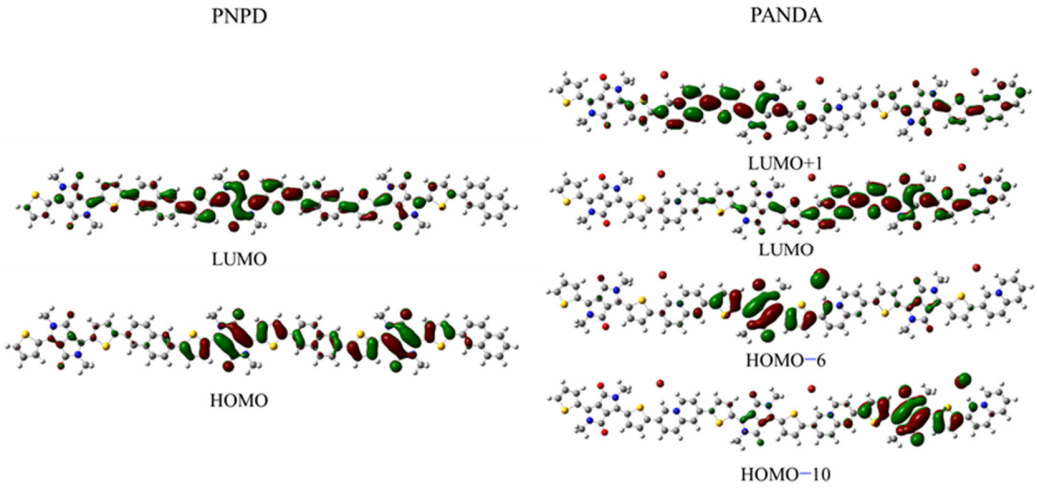

Figure S13. Frontier molecular orbitals of PNPD and PANDA that are responsible for the S_0-S_1 transition. The figure shows that the HOMO and LUMO orbitals of PNPD are delocalized on the whole molecule, which indicates transition process is local excitation with less charge transfer features. The HOMO−6 and HOMO−10 orbitals of PADNA are mostly localized on the DPP fragment, and LUMO and LUMO+1 orbitals are localized on the AN fragment, indicating

that the transition of PANDA is a typical charge transfer absorption from DPP segment to AN segment.

We calculated electronic state transitions and corresponding frontier molecular orbitals of PNPD and PANDA in Figure S12 and Figure S13. It is obvious that transition process is different between PNPD and PANDA. The HOMO and LUMO orbitals of PNPD are delocalized on the whole molecule, which indicates transition process is local excitation with less charge transfer features. The HOMO−6 and HOMO−10 orbitals of PADNA are mostly localized on the DPP fragment, and LUMO and LUMO+1 orbitals are localized on the AN fragment, indicating that the transition of PANDA is a typical charge transfer absorption from DPP segment to AN segment.

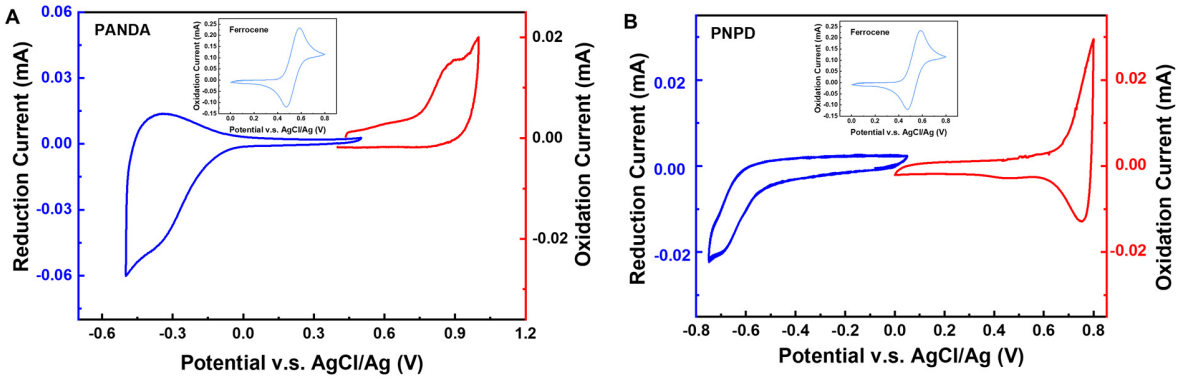

Figure S14. Cyclic voltammograms of the polymers. **A**, PANDA and B, PNPD. Performed in acetonitrile solution with 0.1 M tetrabutylammonium hexafluorophosphate as the supporting electrolyte. $E_{IP,\ PANDA}$ = −5.11 eV, $E_{EA,\ PANDA}$ = −4.21 eV, $E_{IP,\ PNPD}$= −5.01 eV, $E_{EA,\ PNPD}$ = −3.78 eV.

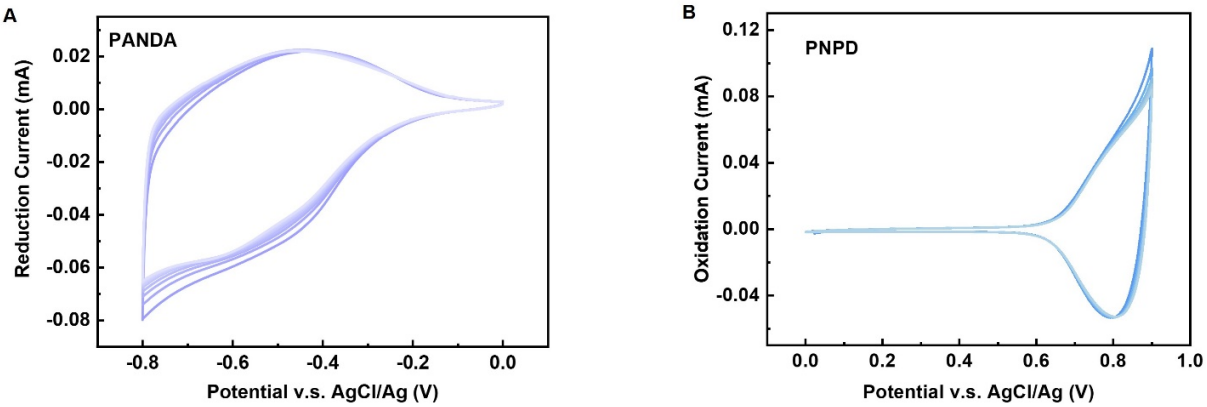

Figure S15. Cycling stability of PANDA (A) and PNPD (B) in 0.1 M NaCl solution. Both PANDA and PNPD show good stability in the cycling test.

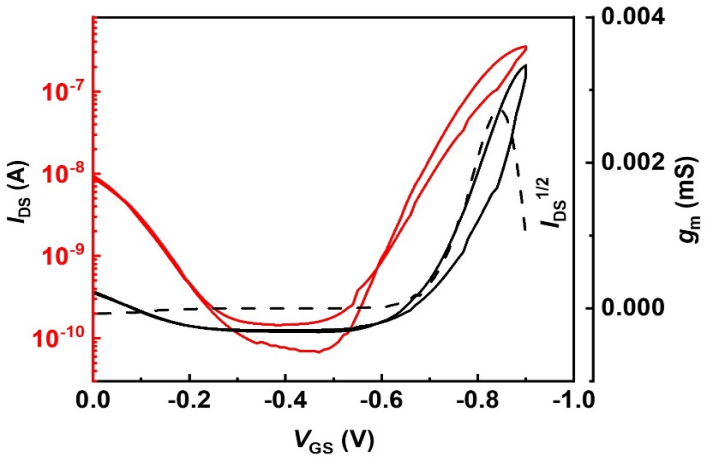

Figure S16. Transfer characteristics of the PNPD OECT devices. Channel dimensions: W/L = 100/10 μm, d = 40 nm. V_{DS} was set to −0.6 V. The red line stands for drain current change, the dashed line is the square root of drain current, and the black solid line stands for transconductance g_m.

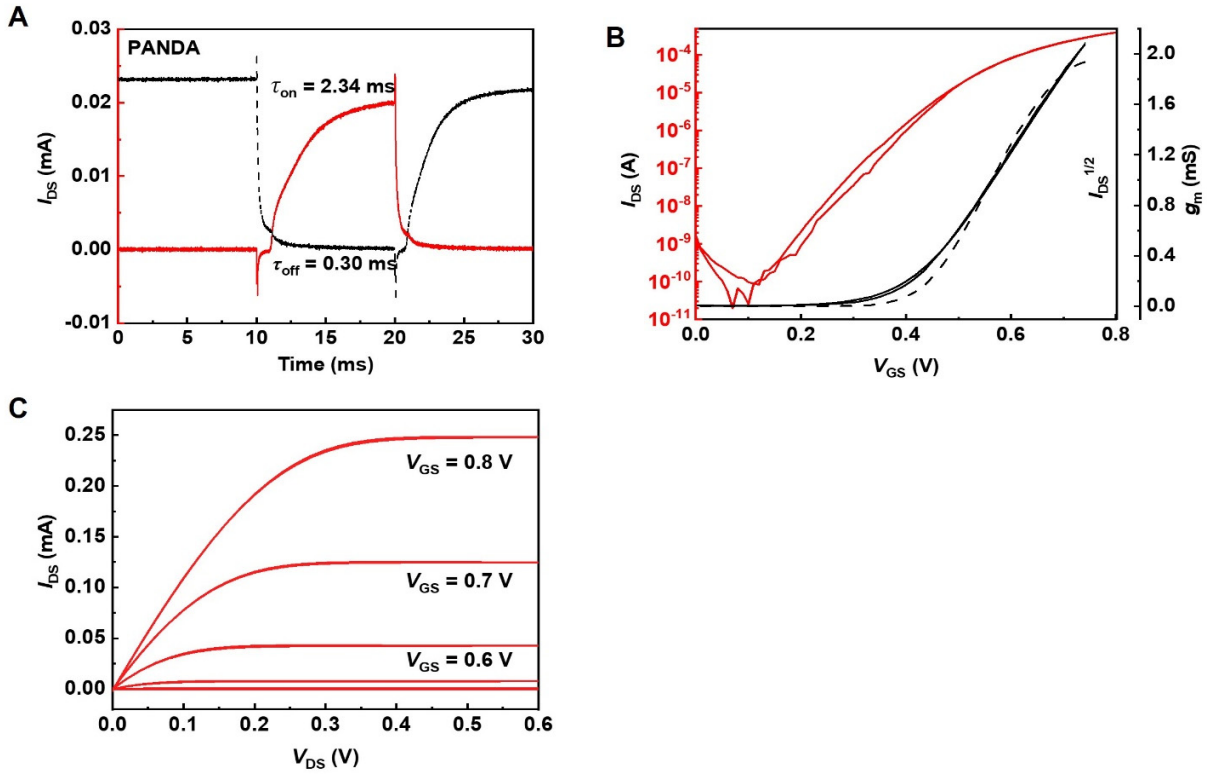

Figure S17. Transient response (A) transfer curve (B) and output characteristics (C) of a typical PANDA OECT device. The device shows steady output properties with high current density.

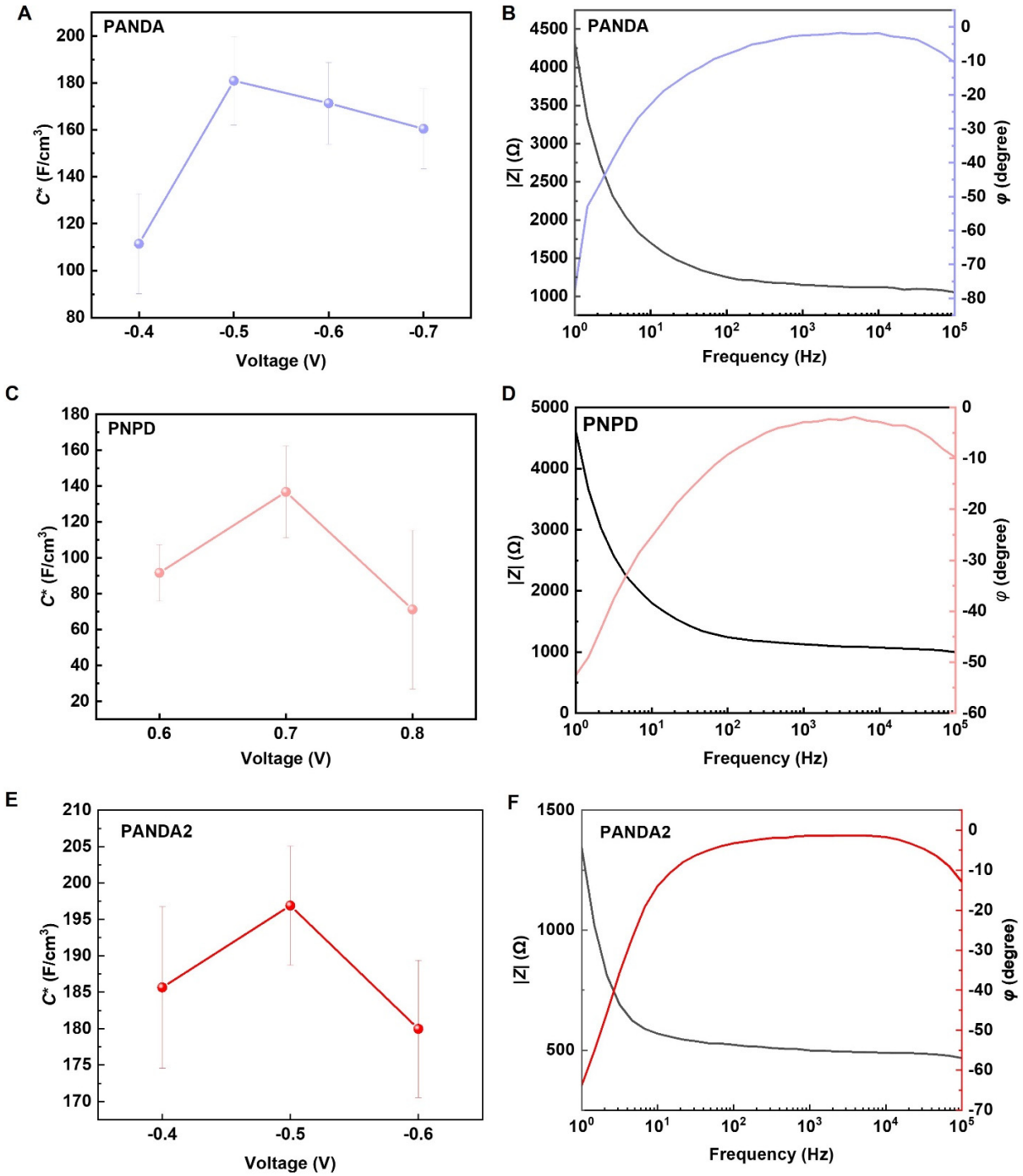

Figure S18. Capacitive behaviors of three polymers. (A, C&E) Voltage-capacitance relationship measured through the electrochemical impedance spectrum (EIS). (B, D&F), The corresponding Bode and phase plot. In the plot, PANDA and PANDA2 was biased at −0.5 V, and PNPD was bias at 0.7 V.

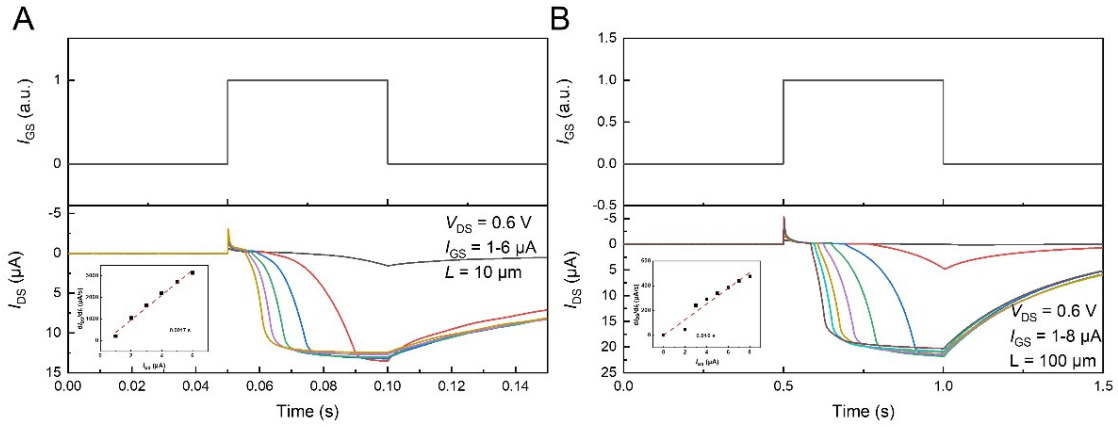

Figure S19 Experimental transient response of PANDA OECTs. Under application of a constant gate current, **A** L = 10 μm, **B** L = 100 μm. (Inset) The transient slope of source-drain current is plotted versus gate current, which predicts τ_e. The gate current measurements method was performed to evaluate the charge carrier mobilities using the equation: $(dI_{DS})/dt=I_{GS}/\tau_e$; $\mu=L^2/(\tau_e \cdot V_{DS})$. [25]

The estimated mobility of our OECT device (W/L = 100/10 μm) is 9.8×10^{-4} cm^2 V^{-1} s^{-1}, which is much lower than the mobilities estimated by μC^*, but is close to the rate of ion migration (Fig. R4 A). As Bernards *et al.* stated in the article, the ion circuit of OECTs is not considered in the model. For devices with a small channel, the distance from the gate to the channel is larger than the channel length. Therefore, it is not accurate to estimate the mobility by the "gate current measurements" method due to the limitation of ion mobility.

Thus, we measured OECT devices with a longer channel length ((W/L = 1000/100 μm), and the estimated mobility is 1.0×10^{-2} cm^2 V^{-1} s^{-1} (Figure S26B). The value is 20 times less than the mobility estimated by μC^*. We think these results are reasonable, considering the negative effect of ion migration and the decrease of charge carrier mobility due to the increase of the channel length. It is reported that the mobility of some p-type polymers measured by gate current methods is an order of magnitude lower than mobility calculated by μC^*[26]. Therefore, we think that the mobility of PANDA we reported is credible.

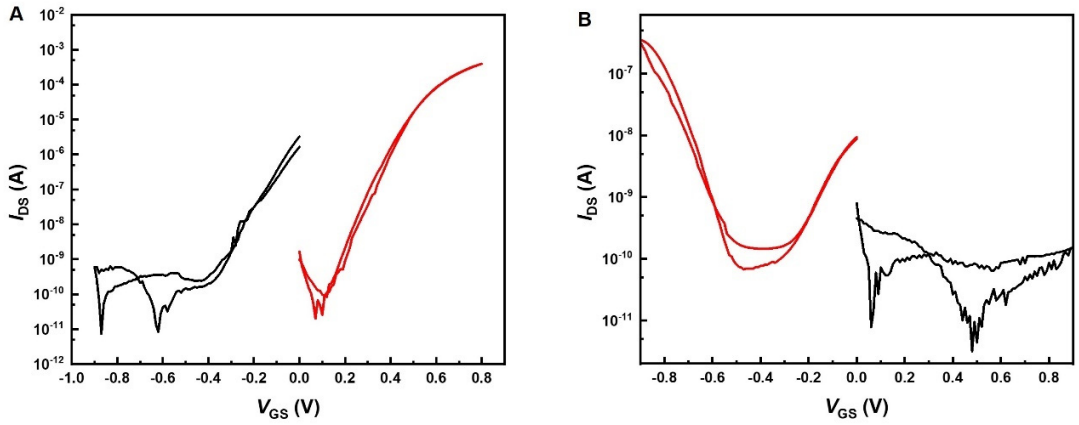

Figure S20. Transfer characteristics of (A) PANDA and (B) PNPD in both p-type and n-type operation regimes. These results demonstrate that PANDA is a pure n-type material while PNPD is a pure p-type material.

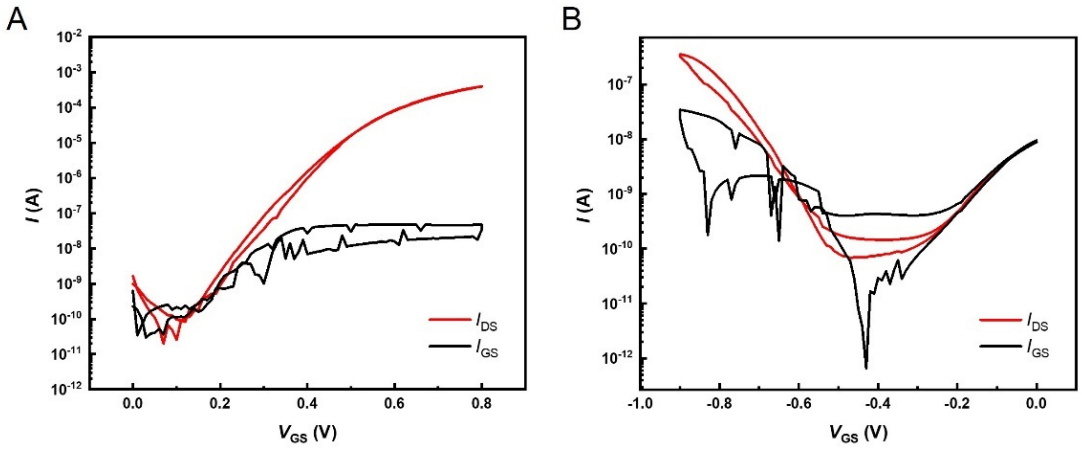

Figure S21. Transfer characteristics and gate leak current of (A) PANDA and (B) PNPD OECT devices.

The gate current (I_{GS}) is four orders of magnitude lower than I_{GS} when the device is switched on for PANDA. Therefore, there is no obvious side reaction during the device operation. Both p-type and n-type OECTs have been well-studied recently. For n-type ones, people usually choose 0~0.8 V for gate voltages and V_{DS}[27]. These voltage ranges are safe for device operation with good cycling stability[28] and will not cause side reactions. The large faradaic efficiency is correlated to the high capacitance of the material, which is normal for OECT materials[16,29]. When the material is functionalized with ethylene glycol chains, the capacitance is effectively increased.

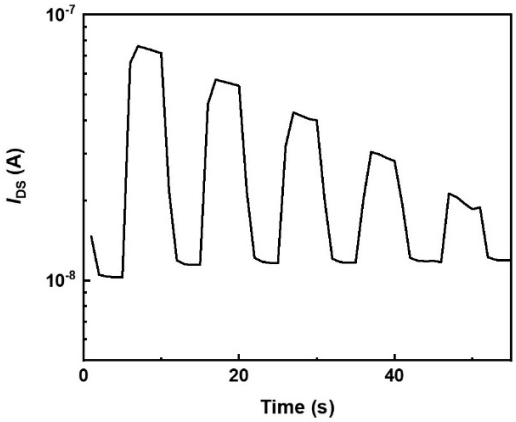

Figure S22. Operational stability of PNPD. PNPD shows a poor stability during on-off cycling.

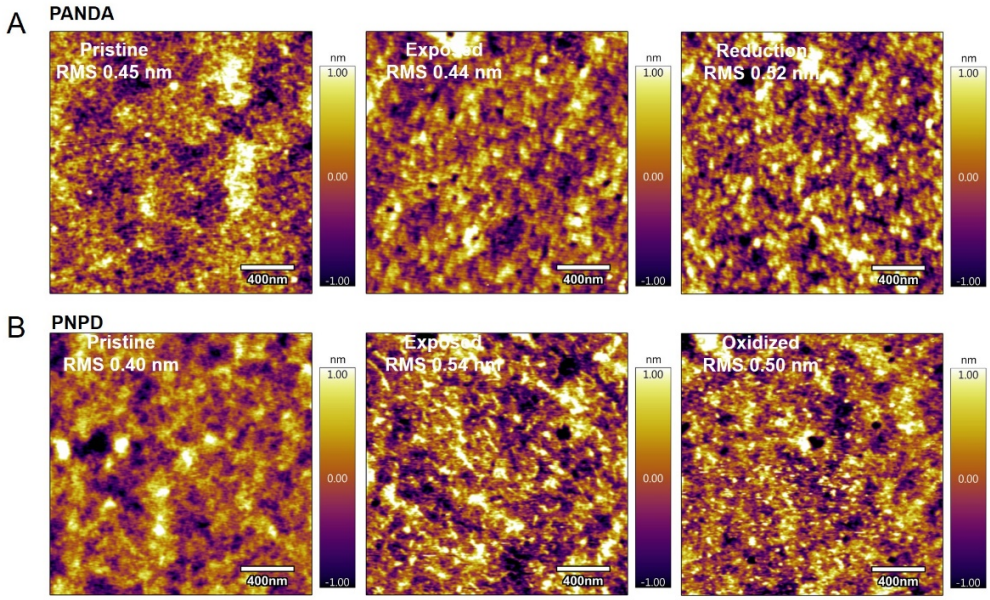

Figure S23. The AFM height images of PANDA and PNPD films. "Pristine" stands for dry films without any treatment. "Exposed" stands for the films immersed in 0.1M NaCl for 10min and blow-dried. "Oxidized/Reduced" stands for the films on the silicon substrate that are oxidized/reduced by voltage bias for 10 min and blow-dried.

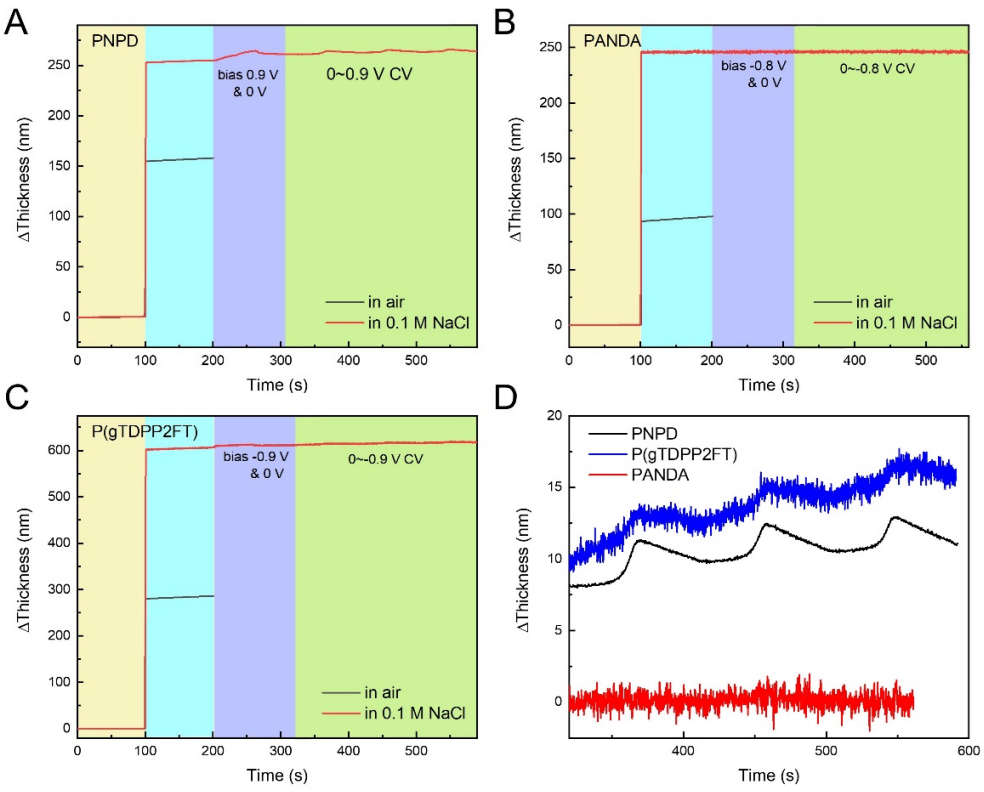

Figure S24. EQCM-D traces recorded for (A) PNPD, (B) PANDA, (C) P(gTDPP2FT). (D) Comparison of active swelling of the three polymers.

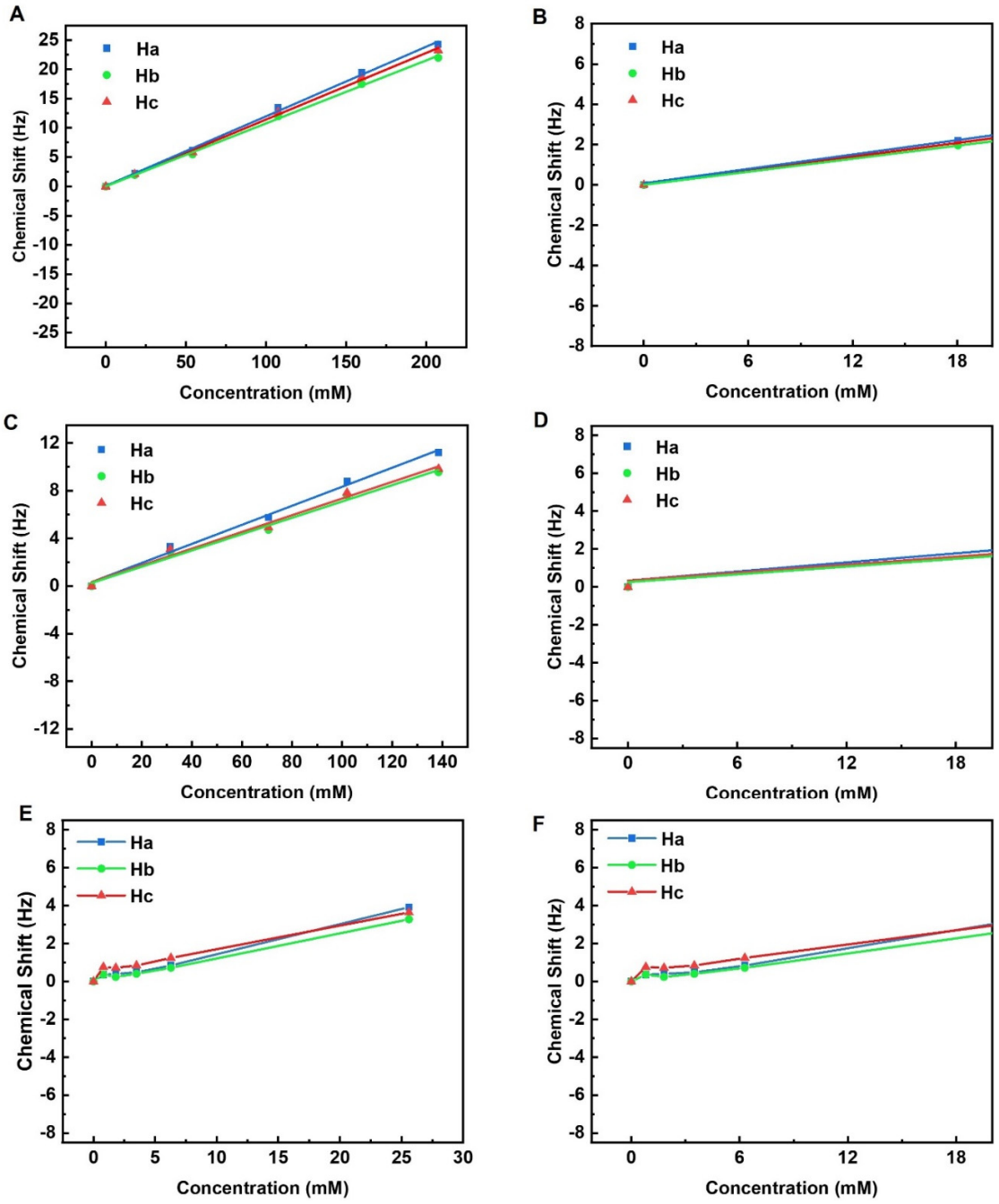

Figure S25. ^{1}H NMR signal shifts of the H atoms on TDPP after adding various amount of tetrabutylammonium salts. A, Full range of the NMR signal changes with variable concentration of tetrabutylammonium chloride. **B**, Enlarged range (0-20 mM) of Figure S13E. **C**, Full range of the NMR signal changes with variable concentration of tetrabutylammonium bromide. **D**, Enlarged range (0-20 mM) of Figure S13C. **E**, Full range of the NMR signal changes with variable concentration of tetrabutylammonium iodide. **F**, Enlarged range (0-20 mM) of Figure S13E.

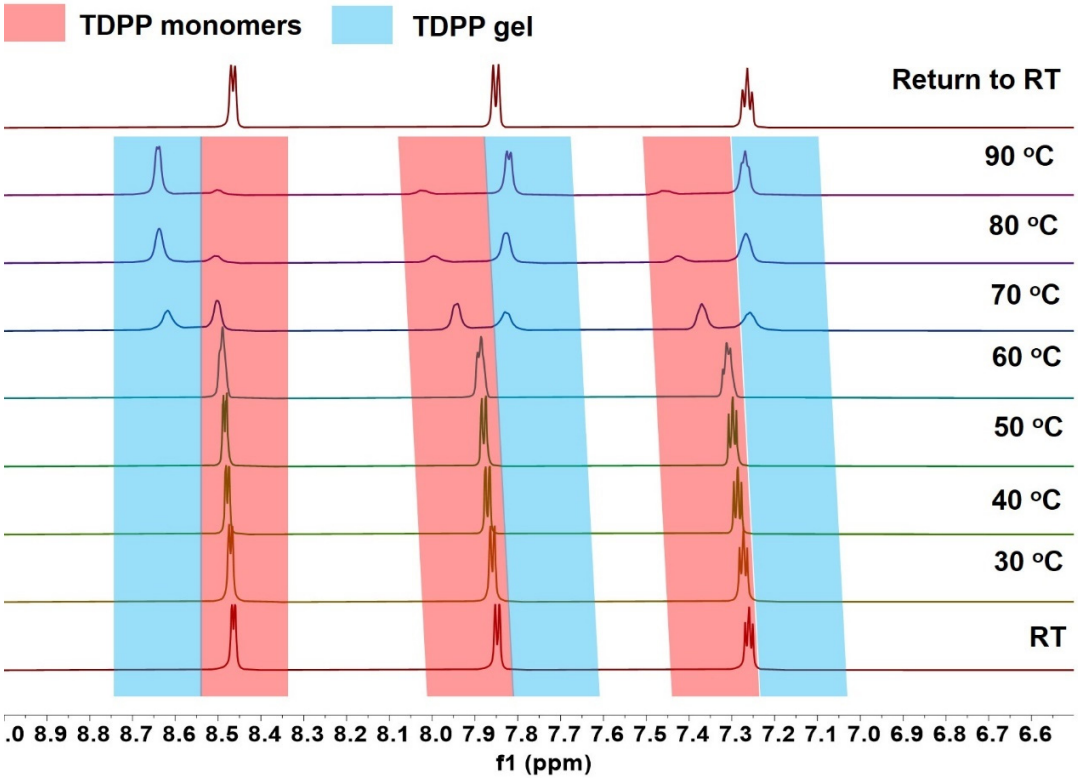

Figure S26. Temperature variable NMR spectrum of TDPP. The red shaded area indicates the peaks from the TDPP monomers, and the blue shaded area indicates a series of new peaks corresponding to aggregates of the TDPP.

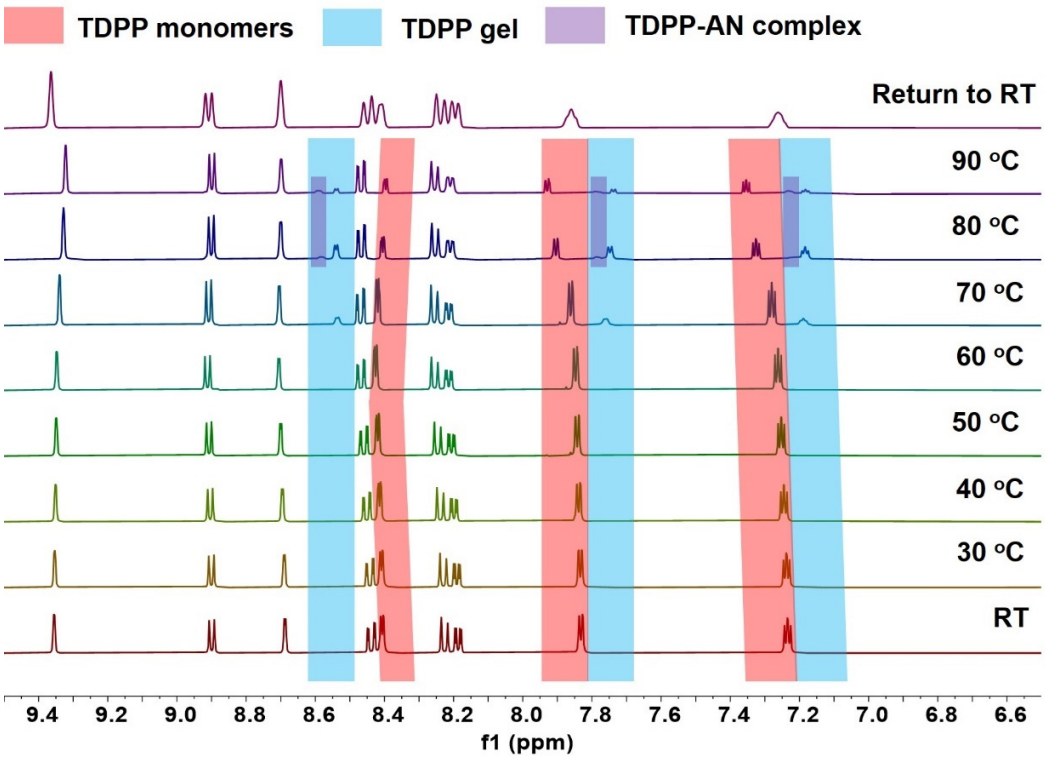

Figure S27. Temperature variable NMR spectrum of TDPP with AN. The red shaded area indicates the hydrogen on the TDPP monomers. The blue shaded area indicates the peaks of the TDPP aggregates. The purple shaded area indicates the new peaks that attributed to the TDPP-AN complex.

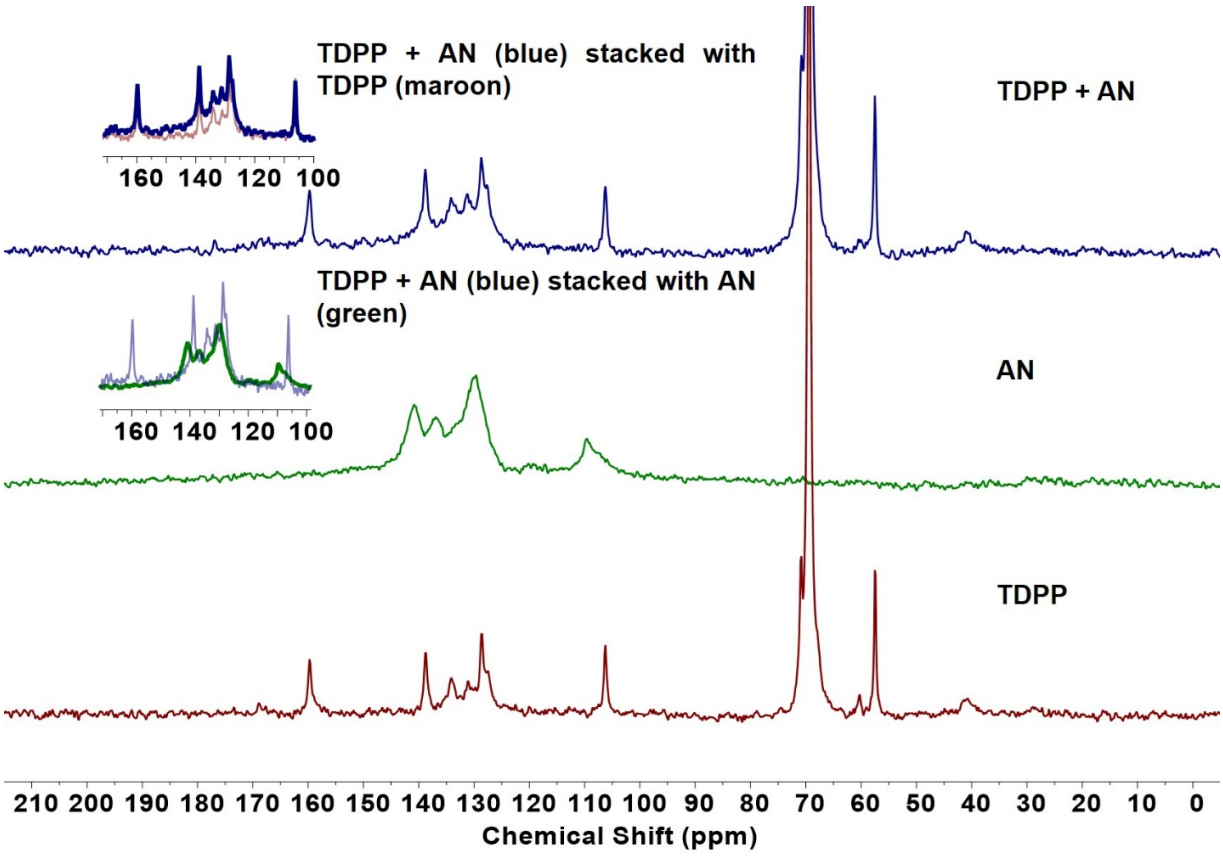

Figure S28. Solid-state NMR spectra of DPP, AN and the DPP-AN mixture (1:1 molar ratio). We used ^{13}C high-power decoupling with magic angle spinning technique for the NMR experiment. With the addition of AN to DPP, the peaks in the range of 120−140 ppm raised dramatically while the peaks between 55 ppm and 78 ppm remain the same as the DPP monomer. When mixed with DPP, the peak of AN at 110 ppm disappear and most of the AN peaks shifted clearly.

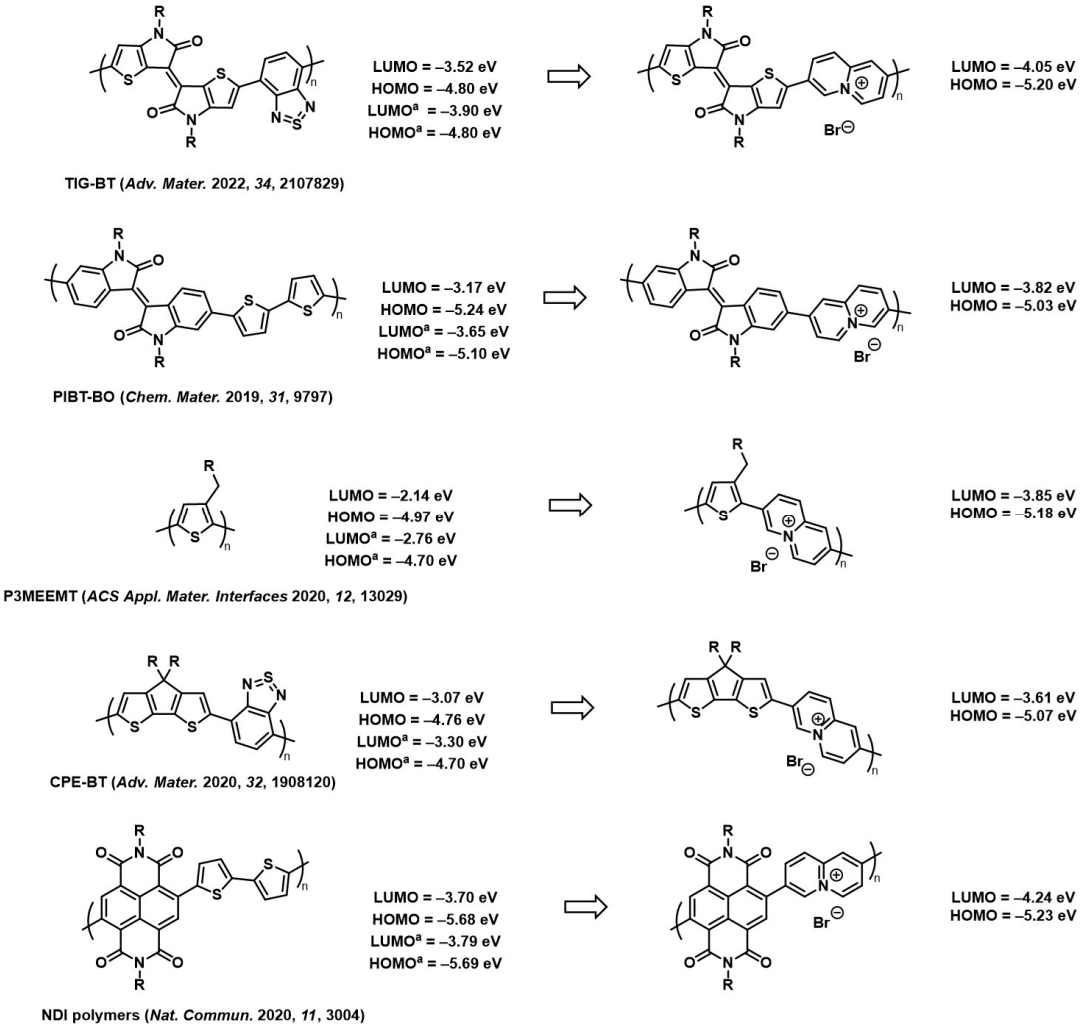

Figure S29 Comparison of the calculated LUMO/HOMO energy levels of the polymers before and after incorporating AN. [a]Experimental values of the LUMO and HOMO energy levels reported in literature..[11,30-33]

Generality and limitations of incorporating AN incorporating AN for other polymers. It has been well demonstrated that all conjugated polymers can transport electrons (n-type), if their LUMO energy level is low enough because low-lying LUMO energy level can provide the polymer with stable negative polarons and well-matched work functions with widely used gold electrodes (*Chem* **2018**, *4*, 2748; *Nature* **2005**, *434*, 194). In a review paper (*Chem. Rev.* **2014**, *114*, 8943), the authors proposed that "the ideal LUMO energy for n-type semiconductors is in the range from −3.6 to −4.5 eV." Therefore, the LUMO energy levels largely determine the charge carrier type in both organic field-effect transistors (OFETs) and organic electrochemical transistors

(OECTs). For example, a typical n-type OECT polymer P-90 with a LUMO energy level of －3.50 eV has shown n-type transport behaviors, though its device performance is low (*Nat. Commun.* **2020**, *11*, 3004). Especially, when LUMO is below －4.00 eV, the materials usually will show better n-type charge transport behaviors.

According to the above conclusions, we performed DFT calculations on more p-type OECT polymers reported in literature, because DFT calculations have been widely used for estimating the energy levels in conjugated polymers and showed good consistency with experimental results (*Phys. Chem. Chem. Phys.* **2019**, *21*, 789). Note that DFT calculations using B3LYP functional often show systematically higher LUMO/HOMO energy levels (0.2~0.4 eV) than the experimental results (CV measurement error: 0.1~0.2 eV) but the trend agrees well with experimental results. Thus, the LUMO levels of polymers can be roughly estimated by DFT calculations.

Figure 29 compares the LUMO/HOMO energy levels of the polymers before and after incorporating AN. The typical p-type polymers usually have LUMO energy levels in the range from －2.0 to－3.6 eV. After incorporating AN, all the polymers show significantly lowered LUMO levels to the range of −3.61 to −4.24 eV. The LUMO levels lowered by 0.47−1.71 eV due to AN's strong electron-deficiency. Therefore, AN unit can greatly lower the LUMO energy levels of the polymers to the required range for n-type polymers and could generally change the polymers from p-type to n-type. Since OECTs work in aqueous media, the much-lowered LUMO energy levels could also provide the polymer with more stable electron transport. In addition, AN is hydrophilic, which can also benefit the ion diffusion/injection in OECT devices as discussed in our manuscript, which cannot be realized by traditional polymer building blocks. However, there are still some restrictions for AN. For example, AN is water soluble and can not be dissolved well in traditional organic solvents, which might limit the molecular weight of AN-based polymers. Moreover, to polymerize with AN, we need the other building block to have tin or boron functional groups for Still or Suzuki polymerization, and thus the synthesis of the other building block is a little bit more complicated.

3. Synthetic Procedure and Characterization

Scheme S1. Synthesis of the monomers and polymers.

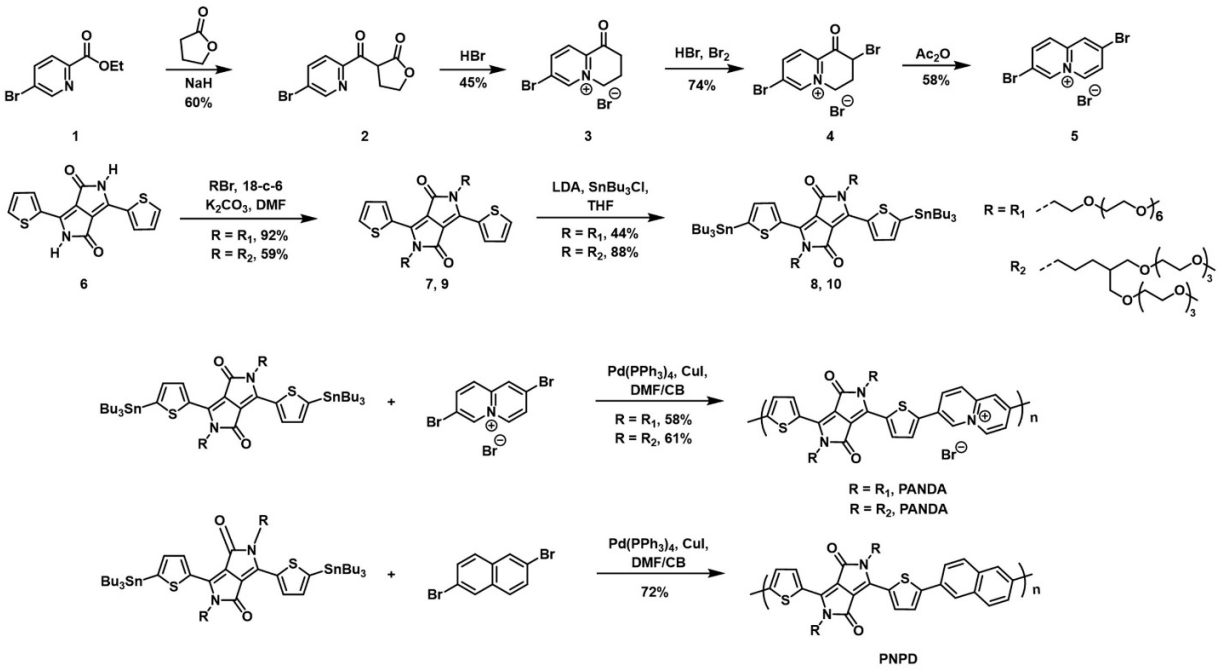

Synthesis of compound 2:

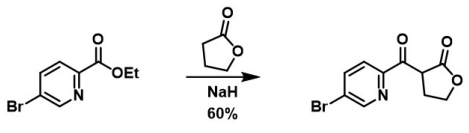

250 mL two-neck bottle was charged with 2.09 g NaH (60% in oil), and the system was degassed. Then 30 mL toluene was injected to the bottle, and then 6.00 g compound 1 (ethyl 5-bromopicolinate) and 2.25 g 1,4-butyrolactone in 20 mL toluene were injected. The mixture was heated to 130 ºC, and we observed a large amount of bubbles. Then heating was continued for 30 min until there were no bubbles. The mixture was quenched with water and exacted with chloroform. The organic phase was combined and dried with sodium sulfonate. The solvent was removed in vacuum, and the residue was purified by column chromatography (petroleum ether:ethyl acetate = 5:1), 4.22 g yellow-colored solid was obtained, yield: 60%. ^{1}H NMR (400 MHz, Chloroform-*d*) δ 8.78 (d, J = 2.2 Hz, 1H), 8.02 – 7.93 (m, 2H), 5.20 – 5.14 (m, 1H), 4.56 (dt, J = 8.7, 4.4 Hz, 1H), 4.45 – 4.39 (m, 1H), 2.80 – 2.73 (m, 1H), 2.61 – 2.53 (m, 1H). ^{13}C NMR (101 MHz, Chloroform-*d*) δ 194.7, 173.4, 150.4, 150.2, 140.0, 139.2, 124.2, 67.3, 46.7, 26.2.

Ketonic form of the isomers is referred above. ESI HRMS calcd. for $[M+H]^+$: 269.9766; found: 269.9754.

Synthesis of compound 3:

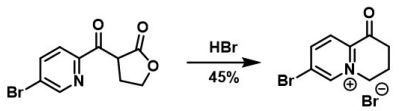

2 3

1.50 g Compound 2 was added to a 100 mL two-necked bottle, then 15 mL 47% HBr solution was added to the system and refluxed at 130 ºC for 10 min. The solution was cooled to room temperature, and 80 mL of deionized water was added to the solution. Then the solution was neutralized by sodium carbonate solution. The mixture was extracted with chloroform. The organic phase was combined and dried with sodium sulfate. Then the mixture was filtered, and the solvent was removed. The resulting solid was dried and then dissolved in 20 mL dichloroethane. The solution was heated to 90 ºC for 3 hours. The precipitates were filtered, washed with dichloromethane, and dried in vacuum. 0.76 g solid was obtained, yield: 45%. δ ^{1}H NMR (400 MHz, Deuterium Oxide) δ 9.29 (d, J = 2.0 Hz, 1H), 8.92 (dd, J = 8.6, 2.0 Hz, 1H), 8.53 (d, J = 8.6 Hz, 1H), 4.95 – 4.92 (m, 2H), 3.06 (t, J = 6.7 Hz, 2H), 2.59 (qd, J = 6.4, 3.9 Hz, 2H). ^{13}C NMR (101 MHz, Deuterium Oxide) δ 189.5, 149.4, 146.8, 127.5, 126.7, 56.8, 34.7, 20.3. ESI HRMS calcd. for $[M \text{ w/o } Br^-]^+$: 225.9862; found: 225.9860.

Synthesis of compound 4:

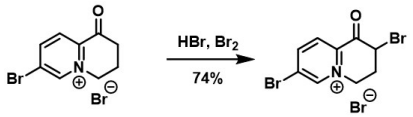

3 4

200 mg compound 3 was dissolved in 47% HBr solution, stirring. Then 104 mg Br_2 in HBr solution was added slowly in 30 min. The mixture was heated at 70 ºC for 2 h, and yellow-colored precipitates were formed and disappeared. The solvent was removed under vacuum, and the resulting solid was recrystallized with ethanol/ethyl acetate giving185 mg yellow-colored solid,

yield: 74%. ^{1}H NMR (400 MHz, Chloroform-*d*) 1H NMR (400 MHz, Deuterium Oxide) ^{1}H NMR (400 MHz, Deuterium Oxide) δ 9.38 (d, J = 1.9 Hz, 1H), 9.13 (dd, J = 11.6, 2.0 Hz, 1H), 8.66 (d, J = 8.7 Hz, 1H), 4.99 (s, 2H), 3.24 (t, J = 7.5 Hz, 1H). ^{13}C NMR (101 MHz, Deuterium Oxide) δ 189.56, 149.41, 146.80, 142.14, 127.52, 126.69, 56.79, 34.74, 20.29. There are three isomers in ^{1}H NMR spectrum, we pick one of them to report. ESI HRMS calcd. for [M w/o Br^-]$^+$: 303.8967; found: 303.8967.

Synthesis of compound 5

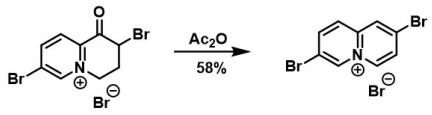

4 5

300 mg compound 4 was added to a round bottle flask, 18 mL acetic anhydride was added as the solvent. The mixture was refluxed for 2 h, and yellow precipitates were formed. The mixture was cooled to room temperature and quenched with 10 mL of deionized water. The solvent was removed under vacuum, and the solid was recrystallized with ethanol. 21 mg brown solid was obtained, yield: 58%. ^{1}H NMR (400 MHz, DMSO-*d*6) δ 9.78 (d, J = 1.8 Hz, 1H), 9.13 (d, J = 7.3 Hz, 1H), 9.02 (d, J = 2.3 Hz, 1H), 8.64 (dd, J = 9.2, 1.8 Hz, 1H), 8.44 (dd, J = 7.2, 2.3 Hz, 1H), 8.40 (d, J = 9.2 Hz, 1H). ^{13}C NMR (101 MHz, DMSO-*d*6) δ 142.1, 141.0, 137.5, 137.4, 132.7, 129.9, 128.3, 127.4, 118.8. ESI HRMS calcd. for [M w/o Br^-]$^+$: 285.8862; found: 285.8843.

Synthesis of compound 7

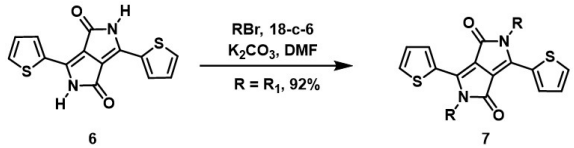

6 7

100 mL two-necked bottle flask was dried and charged with 500 mg compound 6, 1.48 g MPEG7-Br, 481 mg K_2CO_3, and 10 mg 18-crown-6. The system was degassed, and 50 mL NMP was injected. Then the mixture was heated to 130 ^{o}C for 12 hours. The mixture was cooled to room temperature and diluted with water. The solution was extracted with dichloromethane and washed with 2 M HCl. Then the organic phase was combined and dried with sodium sulfonate. The solvent was removed in vacuum, and the residue was purified by column chromatography (ethyl acetate :

methanol = 20:1). 1.45 g deep purple oil was obtained, yield: 92%. ^{1}H NMR (400 MHz, DMSO-*d*6) δ 8.69 (dd, *J* = 3.9, 1.2 Hz, 2H), 8.08 (dd, *J* = 4.9, 1.2 Hz, 2H), 7.39 (dd, *J* = 5.0, 3.9 Hz, 2H), 4.16 (t, *J* = 6.1 Hz, 4H), 3.65 (t, *J* = 6.1 Hz, 4H), 3.53 – 3.39 (m, 48H), 3.23 (s, 6H). ^{13}C NMR (101 MHz, DMSO-*d*6) δ 161.0, 140.2, 134.8, 133.3, 129.6, 129.0, 107.3, 71.8, 70.5, 70.3, 70.3, 70.2, 70.2, 70.1, 68.6, 58.5, 41.9. ESI HRMS calcd. for $[M + Na]^+$: 967.3908; found: 967.3887.

Synthesis of Compound 8

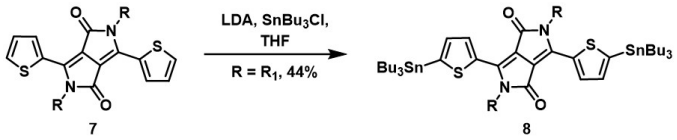

7 8

250 mL two-necked bottle flask was dried in vacuum, then 258 mg compound 7 was added. Both 170 mg $SnBu_3Cl$ and 20 mL THF were added to the flask in a glove box. Then the system was cooled to −110 °C in an ethanol-liquid nitrogen bath. 0.83 mL lithium diisopropyl amide (1 M) was added dropwise, and the system was warmed to −78 °C. Then the mixture was stirred for 3 hours at −78 °C. The mixture was quenched with water and extracted with ethyl acetate. The organic phase was combined and dried with sodium sulfonate. The solvent was removed in vacuum, and the residue was purified by column chromatography (eluent ethyl acetate : triethylamine = 20:1). 185 mg deep purple oil was obtained, yield: 44%. ^{1}H NMR (400 MHz, Chloroform-*d*) δ 8.84 (d, *J* = 3.6 Hz, 2H), 7.24 (d, *J* = 3.7 Hz, 2H), 4.25 (t, *J* = 6.6 Hz, 4H), 3.71 (t, *J* = 6.6 Hz, 4H), 3.60 - 3.51 (s, 44H), 3.49 – 3.45 (m, 4H), 3.30 (s, 6H), 1.58 – 1.46 (m, 12H), 1.34 -1.22 (m, 12H), 1.16 – 1.05 (m, 12H), 0.84 (t, *J* = 7.3 Hz, 18H). ^{13}C NMR (101 MHz, Chloroform-*d*) δ 161.5, 145.9, 139.6, 136.6, 135.6, 135.0, 107.0, 71.9, 70.6, 70.5, 70.5, 70.5, 68.9, 59.0, 41.5, 28.9 27.1, 13.6 11.1. ESI HRMS calcd. for $[M]^+$: 1523.6151; found: 1523.6143.

Synthesis of Compound 10

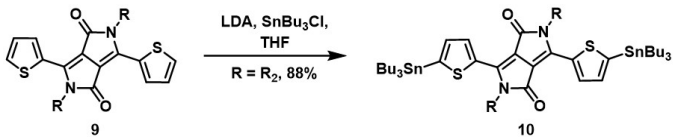

9 10

Synthesis of compound 9 is followed the literature[18], yield 59%. 250 mL two-necked bottle flask was dried in vacuum, then 300 mg compound 9 was added. Both 193 mg $SnBu_3Cl$ and 20 mL THF were added to the flask in a glove box. Then the system was cooled to −110 °C in an ethanol-liquid

nitrogen bath. 0.90 mL lithium diisopropyl amide (1 M) was added dropwise, and the system was warmed to −78 ºC. Then the mixture was stirred for 1 hour at −78 ºC. The mixture was quenched with water and extracted with ethyl acetate. The organic phase was combined and dried with sodium sulfonate. The solvent was removed in vacuum, and the residue was purified by column chromatography (eluent ethyl acetate : triethylamine = 50:1). 402 mg deep purple oil was obtained, yield: 88%. ^{1}H NMR (400 MHz, Chloroform-*d*) δ 9.02 (d, J = 3.7 Hz, 2H), 7.32 (d, J = 3.7 Hz, 2H), 4.08 (t, J = 7.8 Hz, 4H), 3.66 -3.58 (m, 36H), 3.56 - 3.51 (m, 12H), 3.47 - 3.38 (m, 8H), 3.36 (s, 12H), 1.93 – 1.86 (m, 2H), 1.84 - 1.74 (m, 4H), 1.62 - 1.54 (m, 12H), 1.50 – 1.44 (m, 4H), 1.41 – 1.30 (m, 12H), 1.23 – 1.13 (m, 12H), 0.91 (t, J = 7.3 Hz, 18H). ^{13}C NMR (101 MHz, Chloroform-*d*) δ 161.3, 145.8, 139.3, 136.7, 135.9, 135.2, 106.8, 71.9, 71.6, 70.6, 70.6, 70.5, 70.4, 59.0, 42.3, 38.8, 28.9, 28.8, 27.6, 27.2, 25.9, 13.7, 11.1. ESI HRMS calcd. for $[M+H]^{+}$: 1697.7718; found: 1697.7726.

Synthesis of PANDA

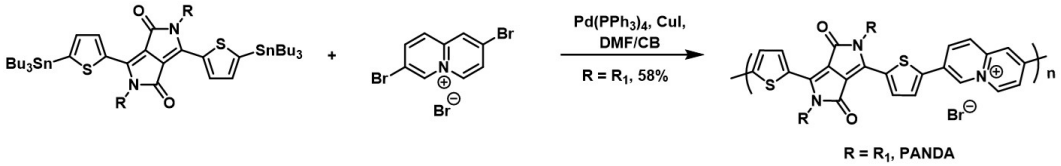

25 mL Schlenk tube was charged with 6.93 mg compound 5 (AN), 0.87 mg $Pd(PPh_3)_4$, 0.14 mg CuI, and then transferred to a glove box. 28.70 mg compound 8 was transferred to the tube with 1 mL CB and 1 mL DMF. Then the tube was sealed and heated to 135 ºC for 12 h. The resulting dark-green solution was poured into methanol and filtered. The polymer was then purified by Soxhlet extraction with hexane, methanol, acetone, and chloroform. The chloroform part was collected and dried. 12.50 mg dark-green solid was obtained, yield: 58%. ^{1}H NMR (400 MHz, Chloroform-*d*) δ 3.63, 3.37. The ^{1}H NMR signal is weak due to the relatively low solubility of PANDA in chloroform.

Synthesis of PNPD

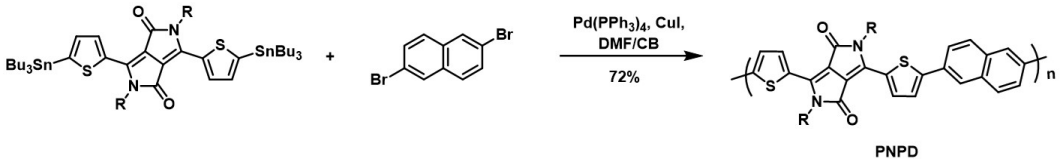

25 mL Schlenk tube was charged with 5.39 mg 2,6-dibromonaphthalene (NP), 0.87 mg $Pd(PPh_3)_4$, 0.14 mg CuI, and then transferred to a glove box. 25.39 mg xompoud 8 was transferred to the tube with 1 mL CB and 1 mL DMF. Then the tube was sealed and heated to 135 ºC for 12 h. The resulting dark-green solution was poured into methanol and filtered. The polymer was then purified by Soxhlet extraction with hexane, methanol, acetone, and chloroform. The chloroform part was collected and dried. 13.80 mg dark-blue solid was obtained, yield: 72%.^{1}H NMR (400 MHz, Chloroform-*d*) δ 8.80, 7.52, 4.31, 3.63, 3.36.

Synthesis of PANDA2

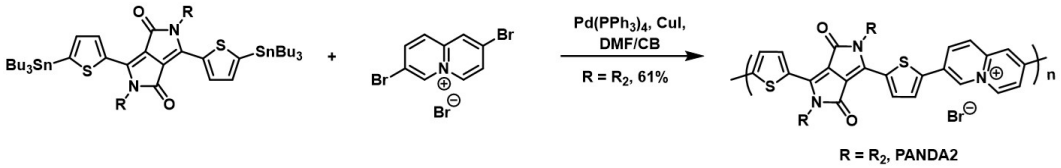

25 mL Schlenk tube was charged with 8.43 mg compound 5 (AN), 1.40 mg $Pd(PPh_3)_4$, 0.22 mg CuI, and then transferred to a glove box. 50.02 mg compound 10 was transferred to the tube with 1 mL CB and 1 mL DMF. Then the tube was sealed and heated to 135 ºC for 12 h. The resulting dark-green solution was poured into methanol and filtered. The polymer was then purified by Soxhlet extraction with hexane, methanol, acetone, and chloroform. The chloroform part was collected and dried. 23.81 mg dark-green solid was obtained, yield: 61%. ^{1}H NMR (400 MHz, Chloroform-*d*) δ 8.91, 8.59, 3.63, 3.35, 1.64.

4. 1H and 13C NMR spectra

Compound 1 ^{1}H NMR spectrum (400 MHz, Chloroform-*d*)

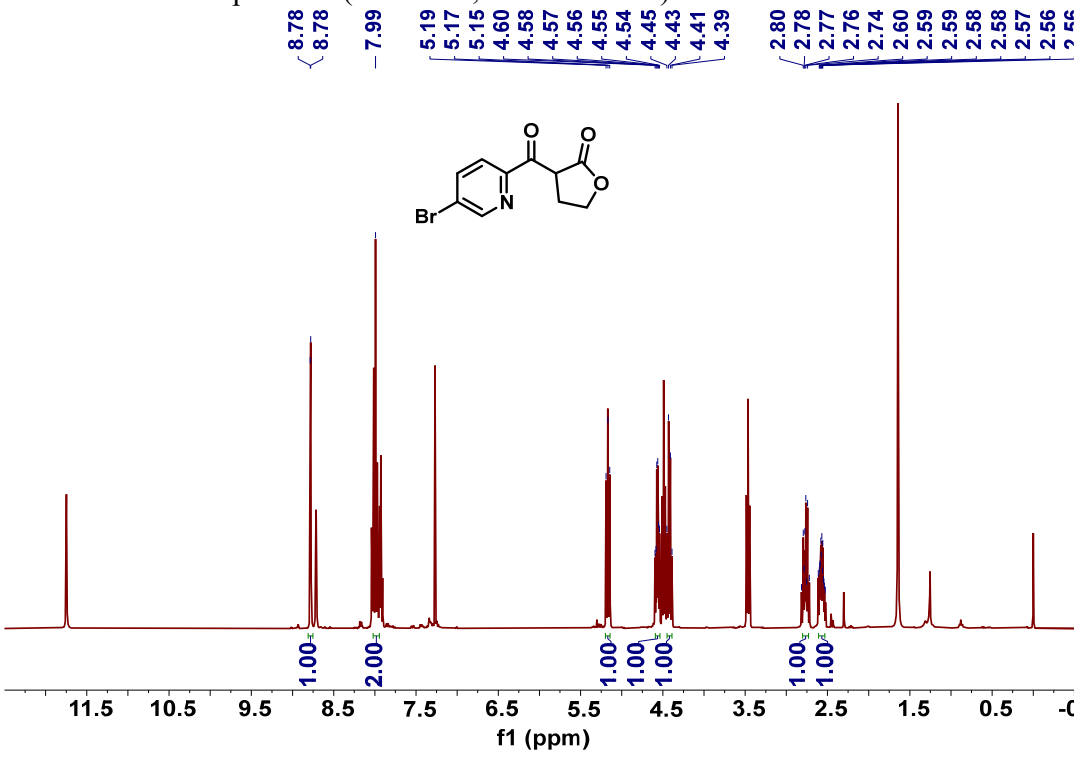

Compound 1 ^{13}C NMR spectrum (101 MHz, Chloroform-*d*)

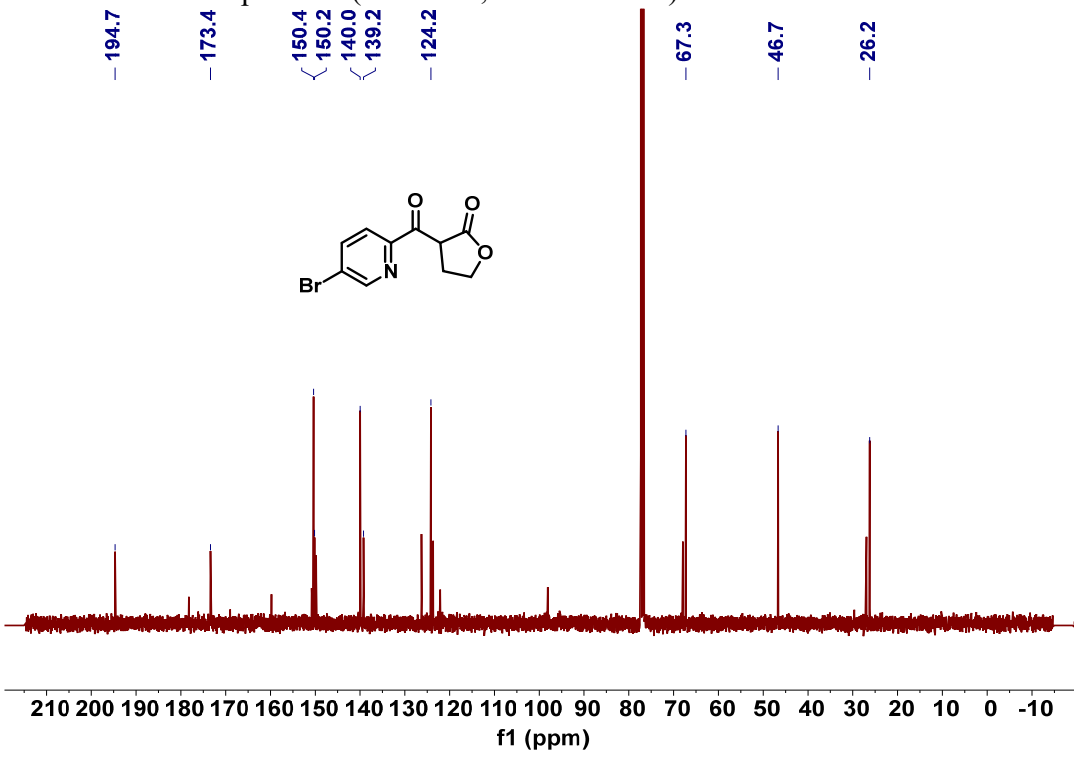

Compound 3 ^{1}H NMR spectrum (400 MHz, Deuterium Oxide)

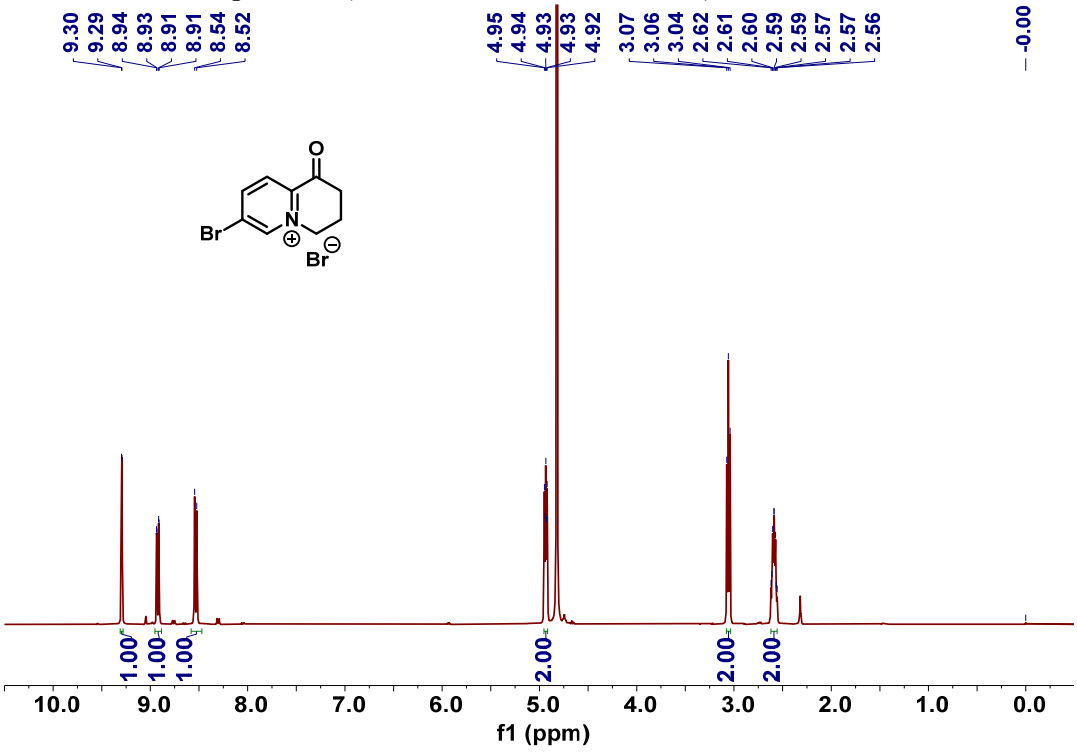

Compound 3 ^{13}C NMR (101 MHz, Deuterium Oxide)

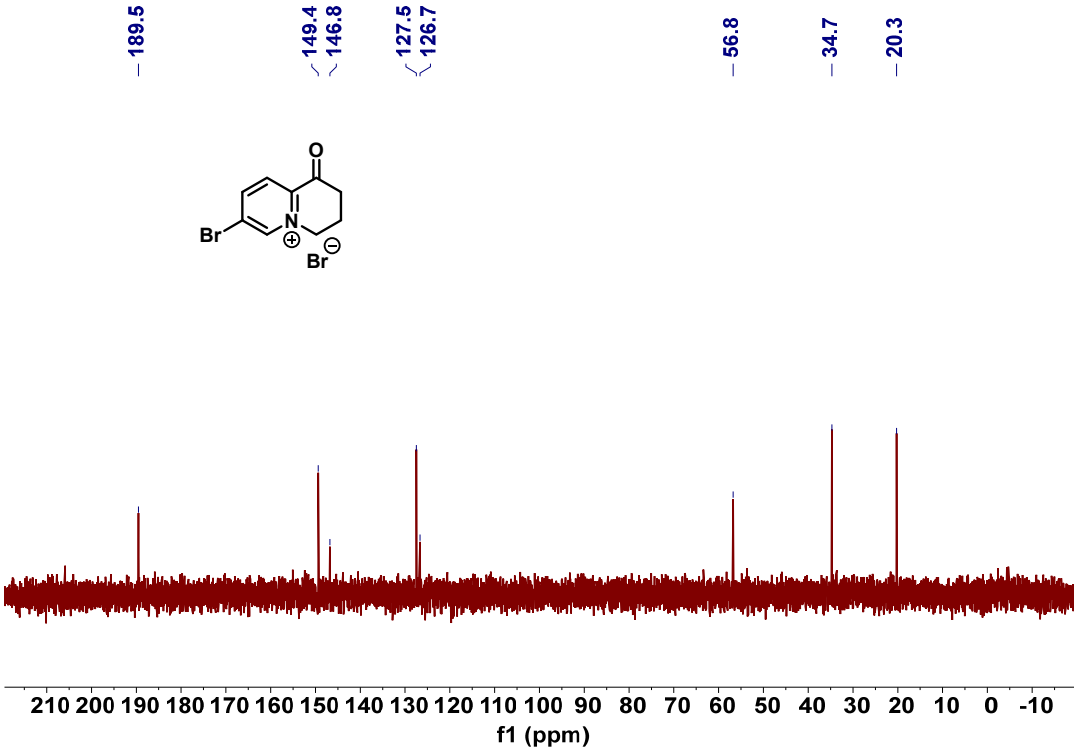

Compound 4 ^{1}H NMR spectrum (400 MHz, Deuterium Oxide)

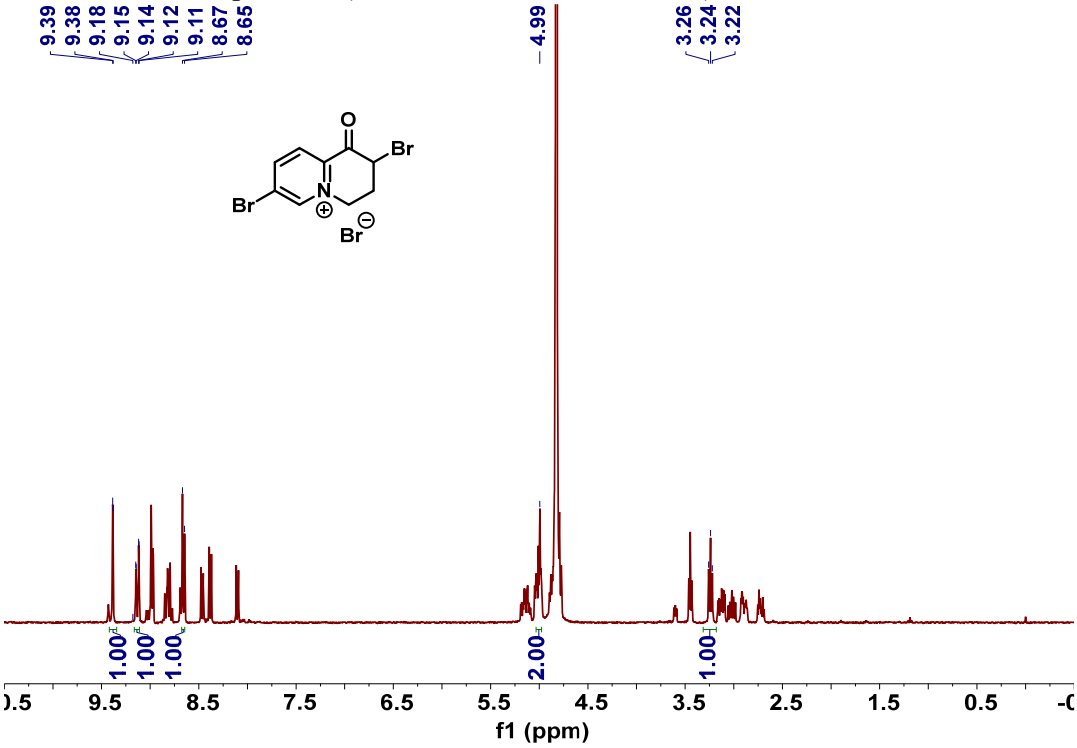

Compound 4 ^{13}C spectrum (101 MHz, Deuterium Oxide)

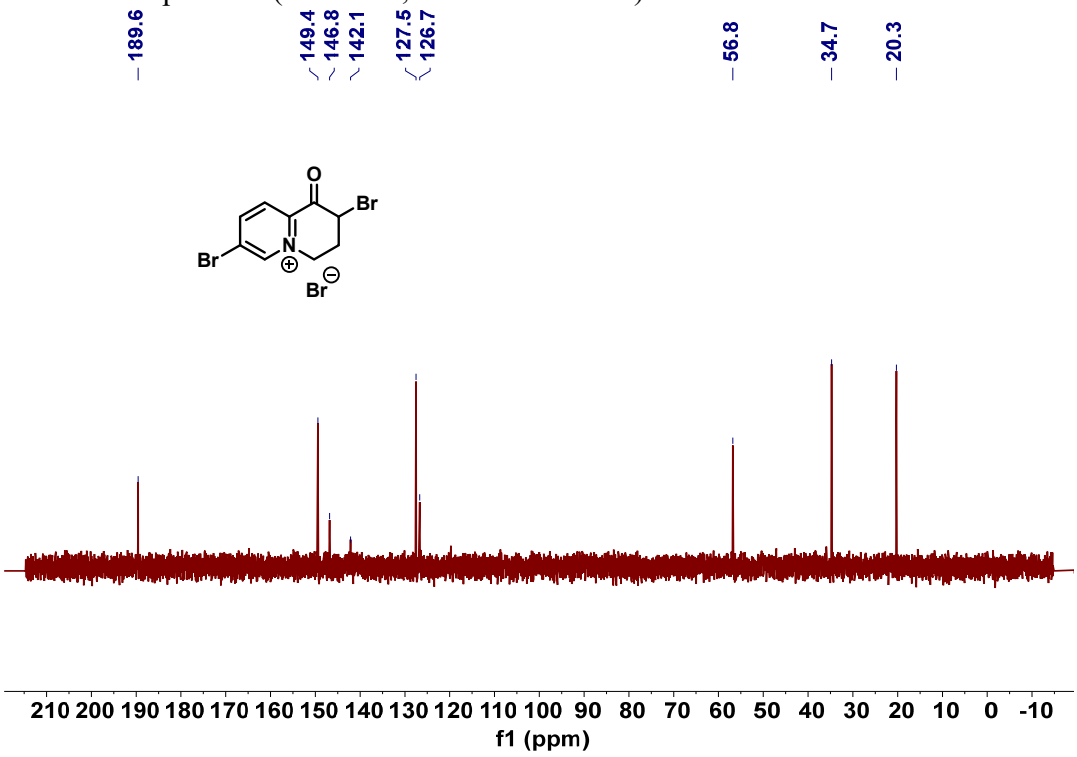

Compound 5 ^{1}H NMR spectrum(4 00 MHz, DMSO-*d*6)

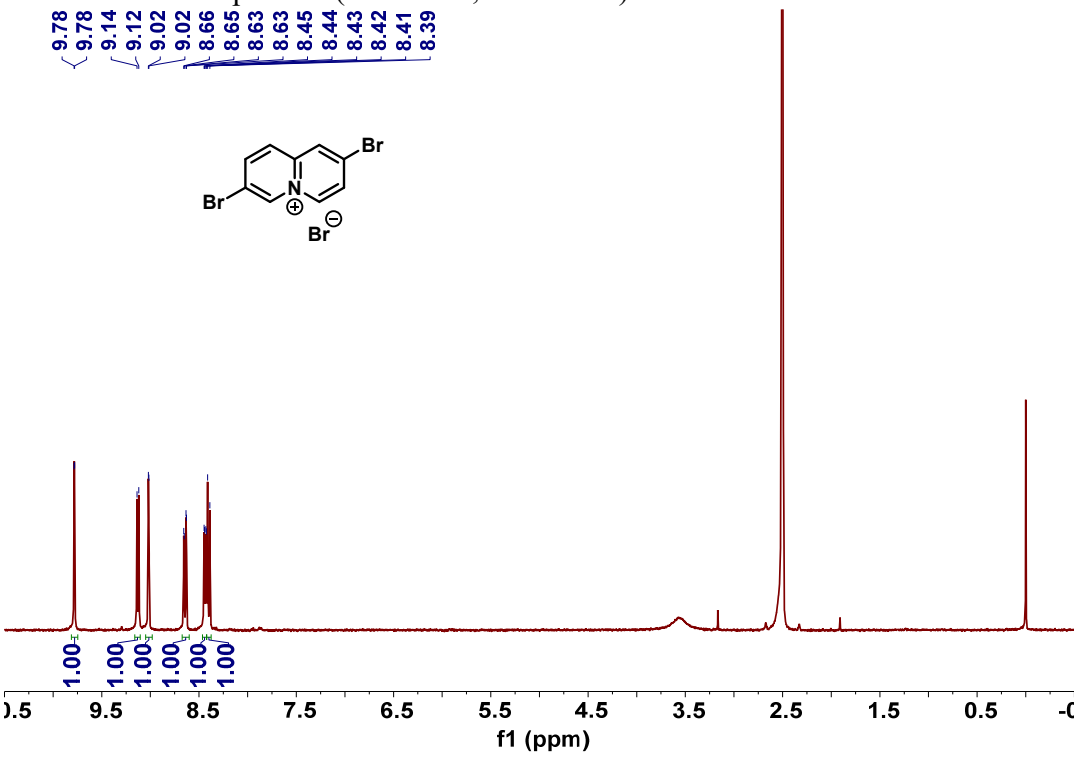

Compound 5 ^{13}C spectrum (101 MHz, DMSO-*d*6)

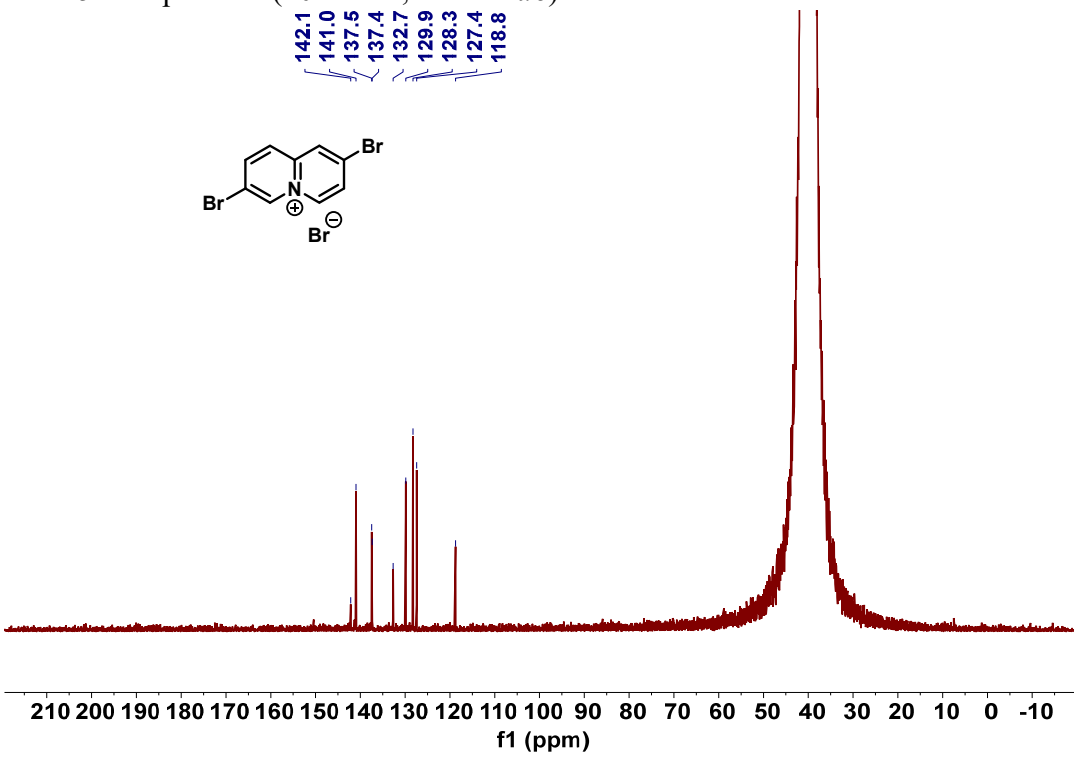

Compound 7 ^{1}H spectrum (400 MHz, DMSO-*d*6)

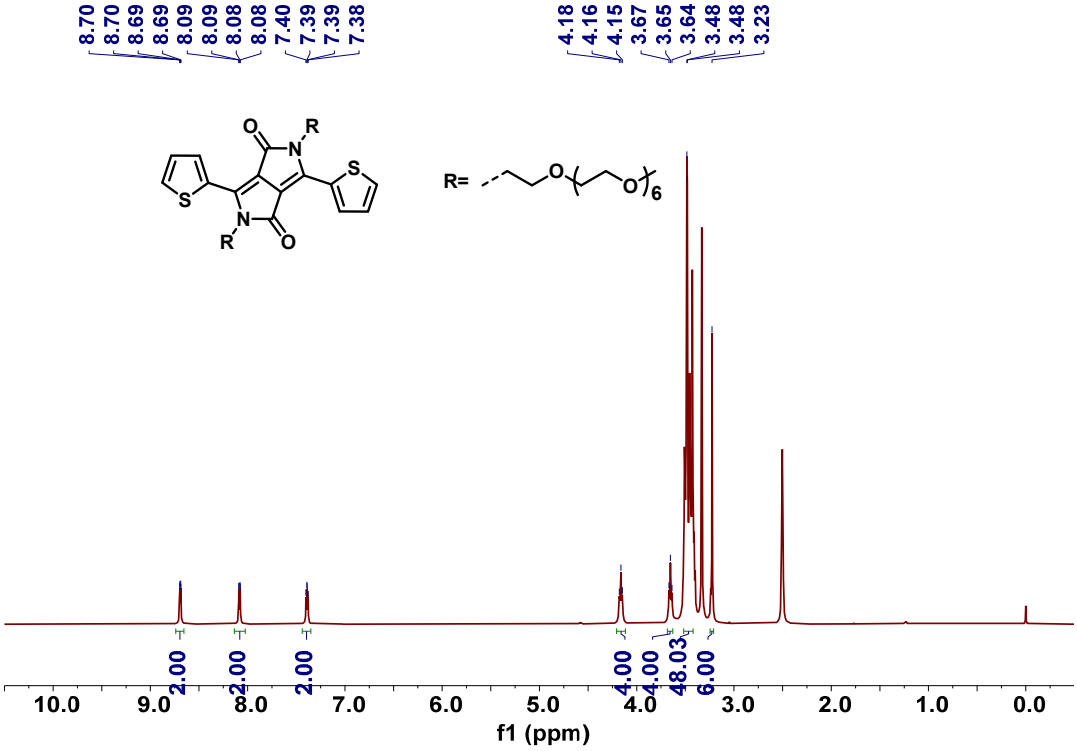

Compound 7 ^{13}C spectrum (101 MHz, DMSO-*d*6)

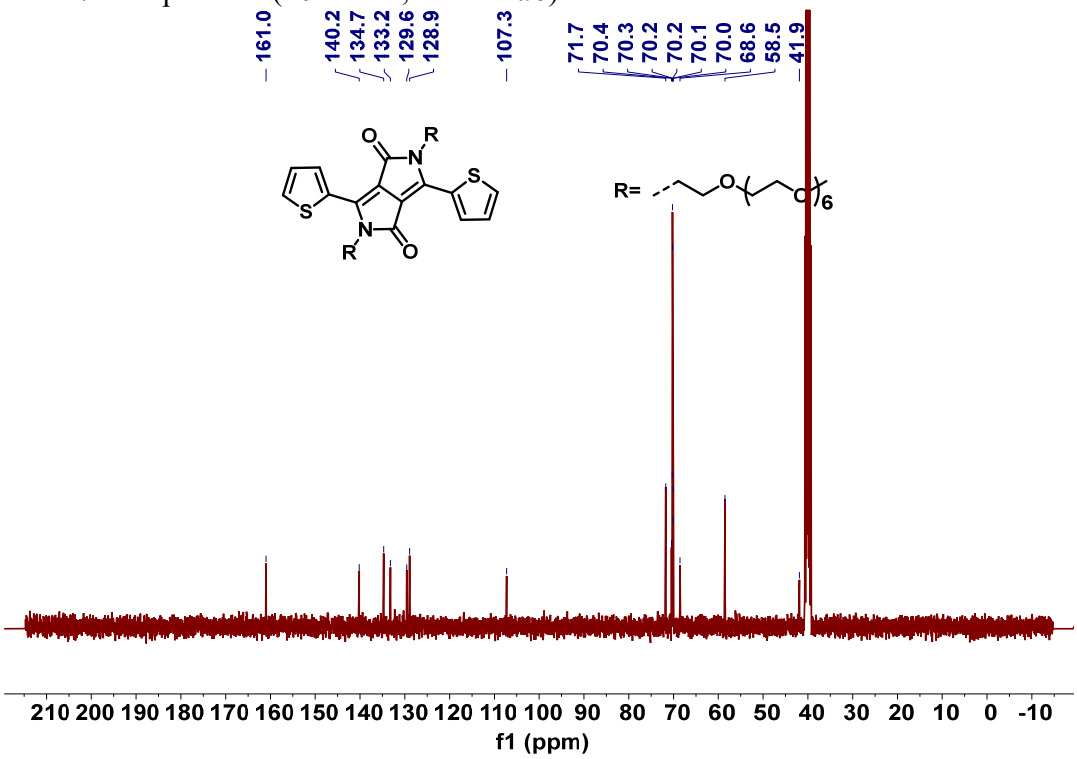

Compound 8 ^{1}H NMR spectrum (400 MHz, Chloroform-*d*)

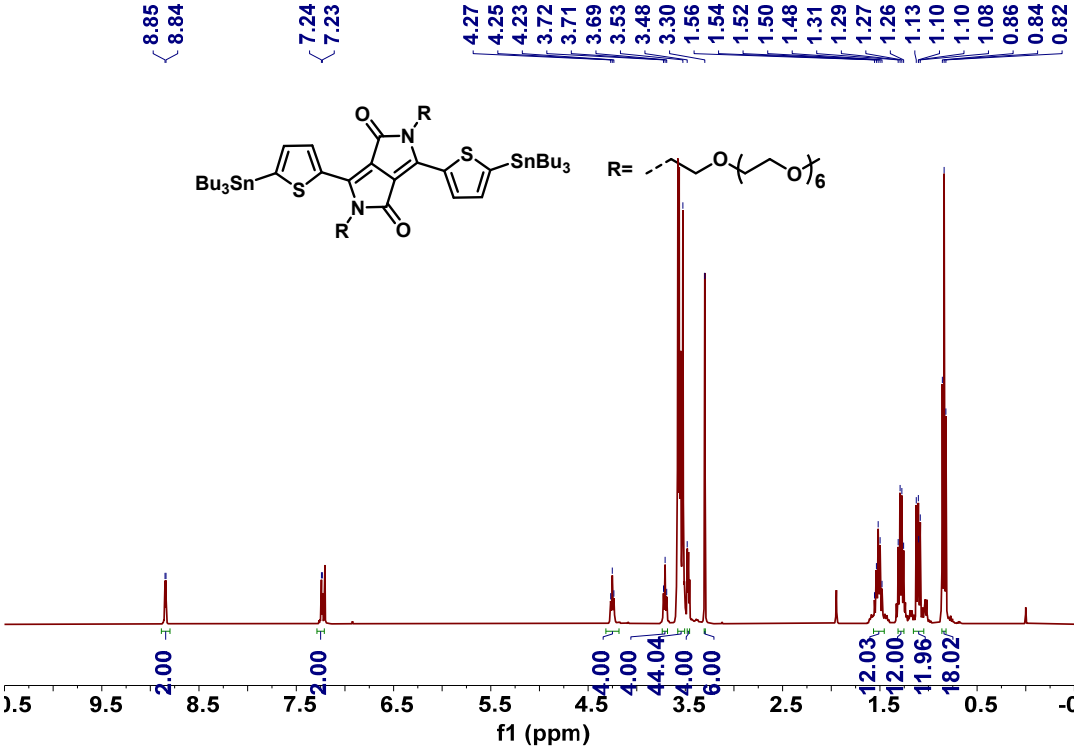

Compound 8 ^{13}C NMR spectrum (101 MHz, Chloroform-*d*)

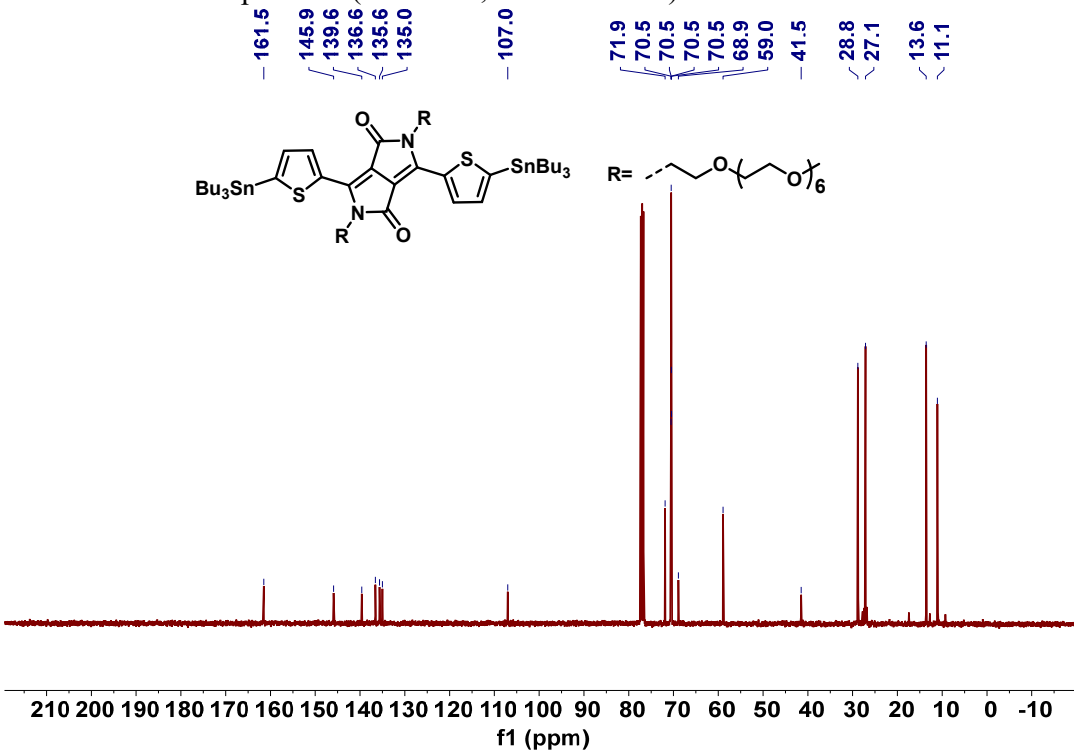

Compound 10 ^{1}H NMR spectrum (400 MHz, Chloroform-*d*)

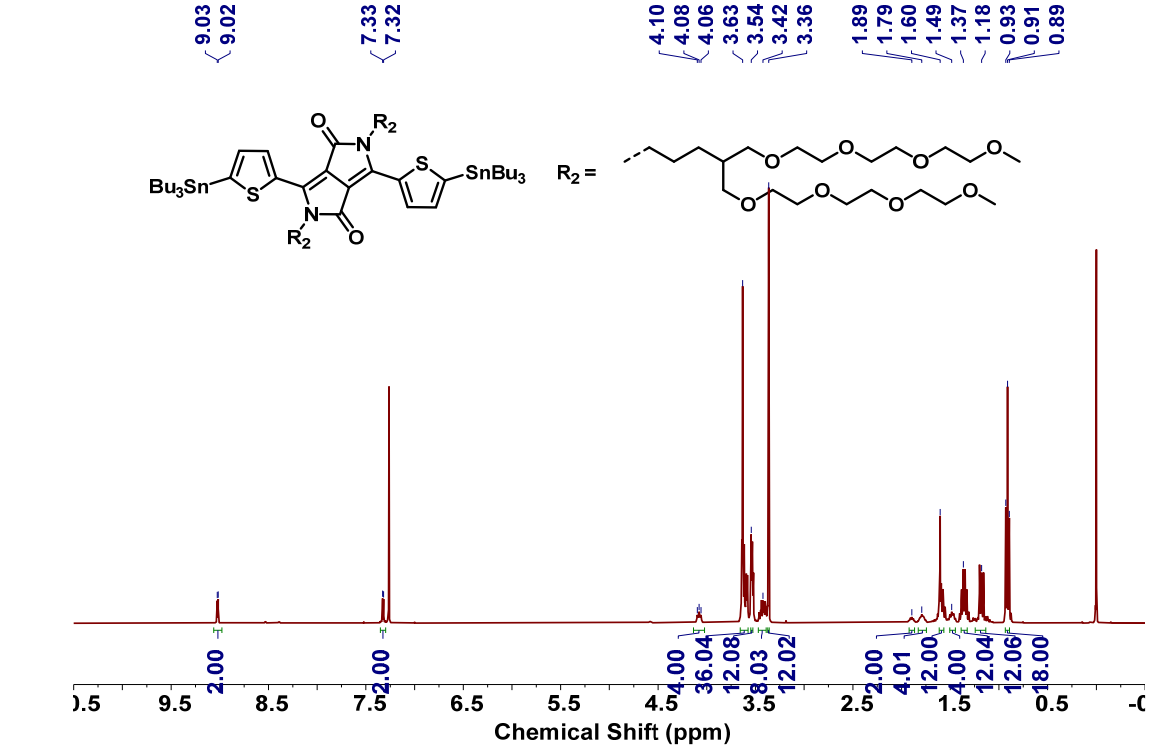

Compound 10 ^{13}C NMR spectrum (101 MHz, Chloroform-*d*)

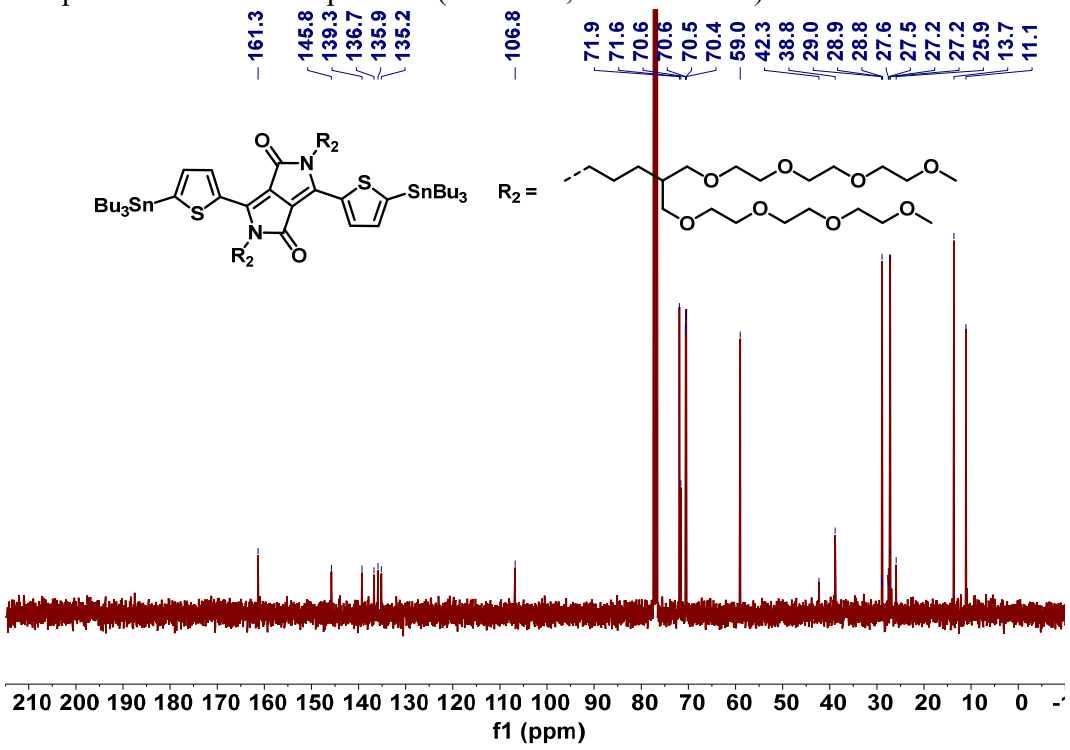

PANDA ^{1}H NMR spectrum (400 MHz, Chloroform-*d*)

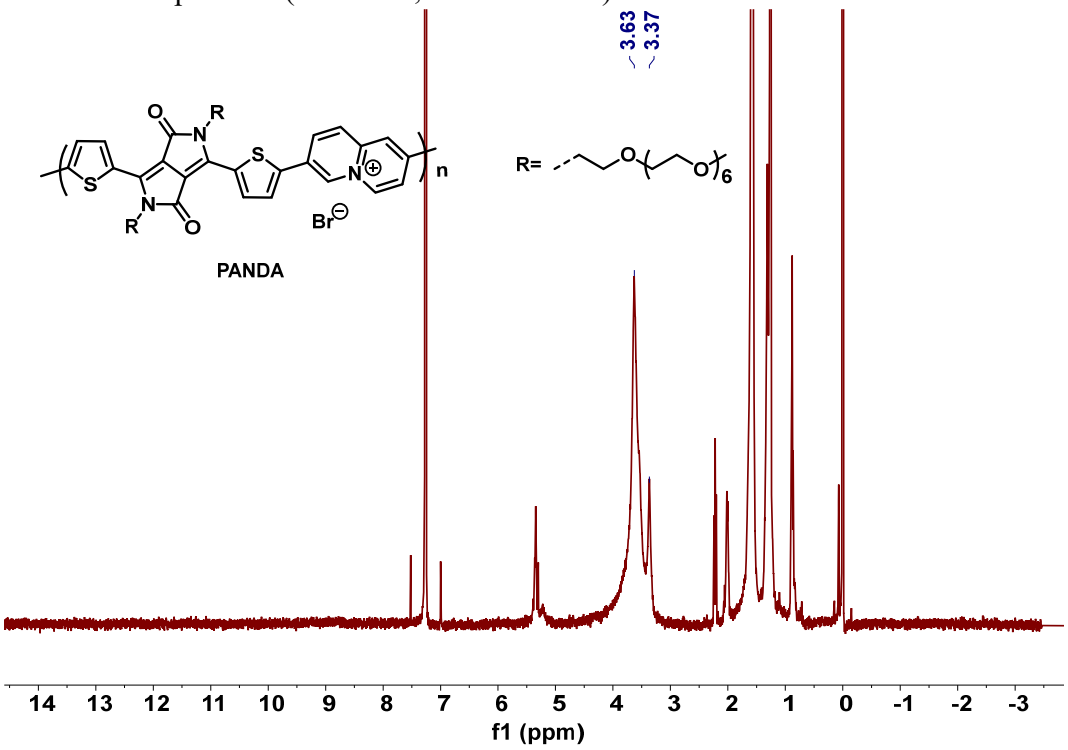

PNPD ^{1}H NMR spectrum (400 MHz, Chloroform-*d*)

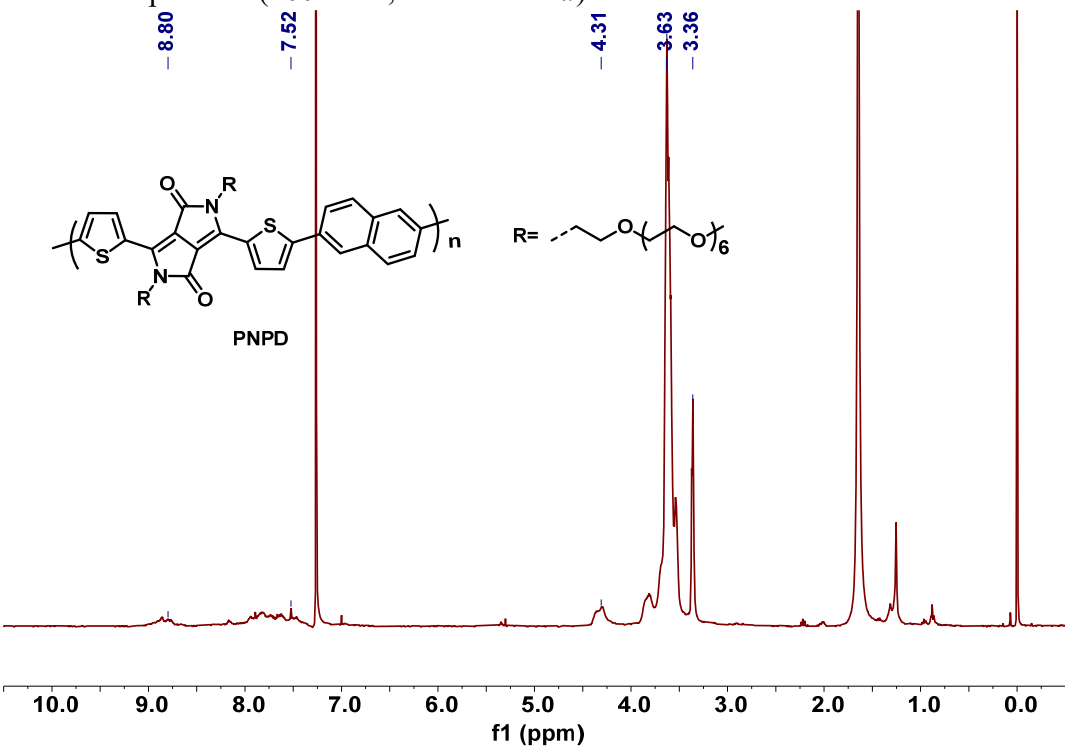

PANDA2 ^{1}H NMR spectrum (400 MHz, Chloroform-*d*)

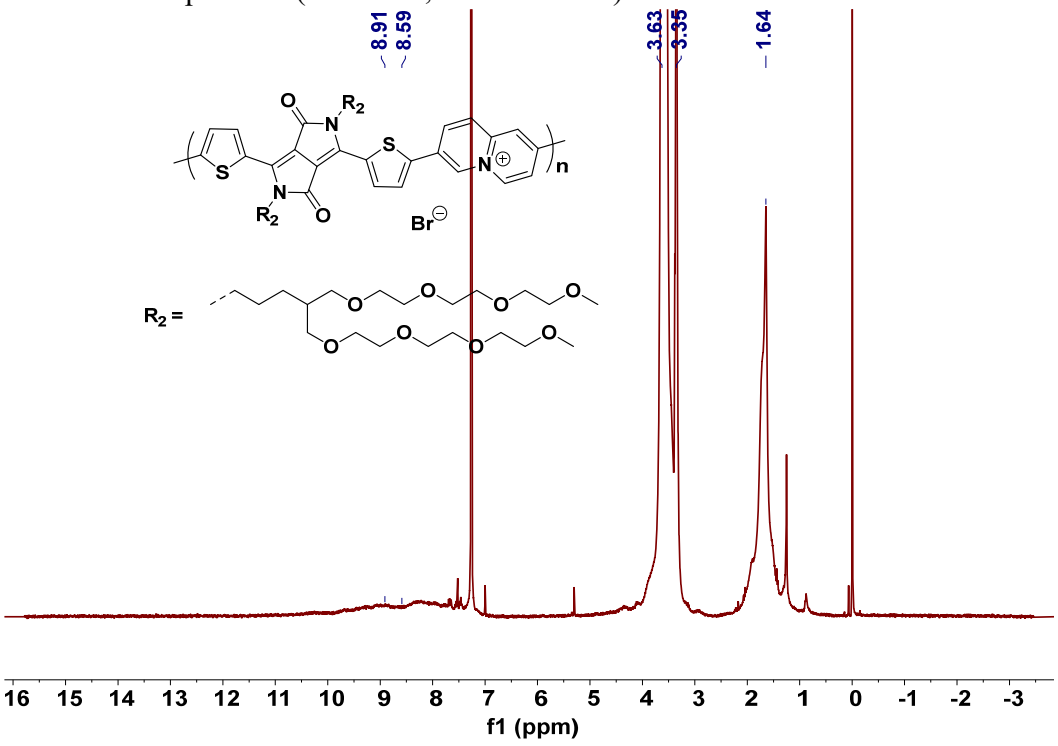

5. Supplementary Reference

1. Frisch, M.J., Trucks, G.W., Schlegel, H.B., Scuseria, G.E., Robb, M.A., Cheeseman, J.R., Scalmani, G., Barone, V., Petersson, G.A., Nakatsuji, H., et al. (2016). Gaussian 16 Rev. B.01.
2. Lu, T., and Chen, F. (2012). Multiwfn: A multifunctional wavefunction analyzer. J. Comput. Chem. *33*, 580-592.
3. Lu, T., and Chen, Q. (2021). Interaction region indicator: a simple real space function clearly revealing both chemical bonds and weak interactions. Chemistry–Methods *1*, 231-239.
4. Humphrey, W., Dalke, A., and Schulten, K. (1996). VMD: Visual molecular dynamics. J. Mol. Graphics *14*, 33-38.
5. Noriega, R., Rivnay, J., Vandewal, K., Koch, F.P.V., Stingelin, N., Smith, P., Toney, M.F., and Salleo, A. (2013). A general relationship between disorder, aggregation and charge transport in conjugated polymers. Nat. Mater. *12*, 1038-1044.
6. Rivnay, J., Noriega, R., Kline, R.J., Salleo, A., and Toney, M.F. (2011). Quantitative analysis of lattice disorder and crystallite size in organic semiconductor thin films. Phys. Rev. B *84*, 045203.
7. Jia, H., Huang, Z., Li, P., Zhang, S., Wang, Y., Wang, J.-Y., Gu, X., and Lei, T. (2021). Engineering donor–acceptor conjugated polymers for high-performance and fast-response organic electrochemical transistors. J. Mater. Chem. C *9*, 4927-4934.
8. Ma, J.C., and Dougherty, D.A. (1997). The Cation−π Interaction. Chem. Rev. *97*, 1303-1324.
9. Giovannitti, A., Nielsen, C.B., Sbircea, D.T., Inal, S., Donahue, M., Niazi, M.R., Hanifi, D.A., Amassian, A., Malliaras, G.G., Rivnay, J., and McCulloch, I. (2016). N-type organic electrochemical transistors with stability in water. Nat. Commun. *7*, 13066-13074.
10. Kawan, M., Hidalgo, T.C., Du, W., Pappa, A.-M., Owens, R.M., McCulloch, I., and Inal, S. (2020). Monitoring supported lipid bilayers with n-type organic electrochemical transistors. Mater.

Horiz. *7*, 2348-2358.
11. Paterson, A.F., Savva, A., Wustoni, S., Tsetseris, L., Paulsen, B.D., Faber, H., Emwas, A.H., Chen, X., Nikiforidis, G., Hidalgo, T.C., et al. (2020). Water stable molecular n-doping produces organic electrochemical transistors with high transconductance and record stability. Nat. Commun. *11*, 3004-3014.
12. Surgailis, J., Savva, A., Druet, V., Paulsen, B.D., Wu, R., Hamidi-Sakr, A., Ohayon, D., Nikiforidis, G., Chen, X., McCulloch, I., et al. (2021). Mixed conduction in an n-type organic semiconductor in the absence of hydrophilic side-chains. Adv. Func. Mater. *31*, 2010165.
13. Chen, X., Marks, A., Paulsen, B.D., Wu, R., Rashid, R.B., Chen, H., Alsufyani, M., Rivnay, J., and McCulloch, I. (2021). N-type rigid semiconducting polymers bearing oligo(ethylene glycol) side chains for high-performance organic electrochemical transistors. Angew. Chem. Int. Ed. *60*, 9368-9373.
14. Ohayon, D., Savva, A., Du, W., Paulsen, B.D., Uguz, I., Ashraf, R.S., Rivnay, J., McCulloch, I., and Inal, S. (2021). Influence of side chains on the n-type organic electrochemical transistor performance. ACS Appl. Mater. Interfaces *13*, 4253-4266.
15. Samuel, J.J., Garudapalli, A., Mohapatra, A.A., Gangadharappa, C., Patil, S., and Aetukuri, N.P.B. (2021). Single-component CMOS-like logic using diketopyrrolopyrrole-based ambipolar organic electrochemical transistors. Adv. Func. Mater. *31*, 2102903.
16. Feng, K., Shan, W., Ma, S., Wu, Z., Chen, J., Guo, H., Liu, B., Wang, J., Li, B., Woo, H.Y., et al. (2021). Fused bithiophene imide dimer-based n-type polymers for high-performance organic electrochemical transistors. Angew. Chem. Int. Ed. *60*, 24198-24205.
17. Feng, K., Shan, W., Wang, J., Lee, J.W., Yang, W., Wu, W., Wang, Y., Kim, B.J., Guo, X., and Guo, H. (2022). Cyano-functionalized n-type polymer with high electron mobility for high-performance organic electrochemical transistors. Adv. Mater. *34*, e2201340.
18. Li, P., Shi, J., Lei, Y., Huang, Z., and Lei, T. (2022). Switching p-type to high-performance n-type organic electrochemical transistors via doped state engineering. Nat. Commun. *13*, 5970-5977.
19. Shi, J., Li, P., Deng, X.-Y., Xu, J., Huang, Z., Lei, Y., Wang, Y., Wang, J.-Y., Gu, X., and Lei, T. (2022). Revealing the role of polaron distribution on the performance of n-type organic electrochemical transistors. Chem. Mater. *34*, 864-872.
20. Zhang, Y., Ye, G., van der Pol, T.P.A., Dong, J., van Doremaele, E.R.W., Krauhausen, I., Liu, Y., Gkoupidenis, P., Portale, G., Song, J., et al. (2022). High-Performance Organic Electrochemical Transistors and Neuromorphic Devices Comprising Naphthalenediimide-Dialkoxybithiazole Copolymers Bearing Glycol Ether Pendant Groups. Adv. Func. Mater. *32*, 2201593.
21. Wu, H.Y., Yang, C.Y., Li, Q., Kolhe, N.B., Strakosas, X., Stoeckel, M.A., Wu, Z., Jin, W., Savvakis, M., Kroon, R., et al. (2022). Influence of Molecular Weight on the Organic Electrochemical Transistor Performance of Ladder-Type Conjugated Polymers. Adv. Mater. *34*, e2106235.
22. Rashid, R.B., Du, W., Griggs, S., Maria, I.P., McCulloch, I., and Rivnay, J. (2021). Ambipolar inverters based on cofacial vertical organic electrochemical transistor pairs for biosignal amplification. Sci. Adv. *7*, eabh1055.
23. Crawford, A.G., Dwyer, A.D., Liu, Z., Steffen, A., Beeby, A., Pålsson, L.-O., Tozer, D.J., and Marder, T.B. (2011). Experimental and Theoretical Studies of the Photophysical Properties of 2- and 2,7-Functionalized Pyrene Derivatives. J. Am. Chem. Soc. *133*, 13349-13362.
24. Miao Xiong, X.Y., Jia-Tong Li, Song Zhang, Zhiqiang Cao, Nathaniel Prine, Yang Lu, Jie-

YuWang, Xiaodan Gu, and Ting Lei* (2021). Efficient n-Doping of Polymeric Semiconductors through Controlling the Dynamics. Angew. Chem. Int. Ed. *60*, 8189-8197.
25. Bernards, D.A., and Malliaras, G.G. (2007). Steady-state and transient behavior of organic electrochemical transistors. Adv. Func. Mater. *17*, 3538-3544.
26. Inal, S., Malliaras, G.G., and Rivnay, J. (2017). Benchmarking organic mixed conductors for transistors. Nat. Commun. *8*, 1767-1773.
27. Sun, H., Vagin, M., Wang, S., Crispin, X., Forchheimer, R., Berggren, M., and Fabiano, S. (2018). Complementary logic circuits based on high-performance n-type organic electrochemical transistors. Adv. Mater. *30*, 1704916.
28. Stein, E., Nahor, O., Stolov, M., Freger, V., Petruta, I.M., McCulloch, I., and Frey, G.L. (2022). Ambipolar blend-based organic electrochemical transistors and inverters. Nat. Commun. *13*, 5548-5557.
29. Moser, M., Savva, A., Thorley, K., Paulsen, B.D., Hidalgo, T.C., Ohayon, D., Chen, H., Giovannitti, A., Marks, A., Gasparini, N., et al. (2021). Polaron delocalization in donor-acceptor polymers and its impact on organic electrochemical transistor performance. Angew. Chem. Int. Ed. *60*, 7777-7785.
30. Parr, Z.S., Borges-Gonzalez, J., Rashid, R.B., Thorley, K.J., Meli, D., Paulsen, B.D., Strzalka, J., Rivnay, J., and Nielsen, C.B. (2022). From p- to n-type mixed conduction in isoindigo-based polymers through molecular design. Adv. Mater. *34*, e2107829.
31. Wang, Y., Zeglio, E., Liao, H., Xu, J., Liu, F., Li, Z., Maria, I.P., Mawad, D., Herland, A., McCulloch, I., and Yue, W. (2019). Hybrid alkyl–ethylene glycol side chains enhance substrate adhesion and operational stability in accumulation mode organic electrochemical transistors. Chem. Mater. *31*, 9797-9806.
32. Schmode, P., Savva, A., Kahl, R., Ohayon, D., Meichsner, F., Dolynchuk, O., Thurn-Albrecht, T., Inal, S., and Thelakkat, M. (2020). The Key Role of Side Chain Linkage in Structure Formation and Mixed Conduction of Ethylene Glycol Substituted Polythiophenes. ACS Appl. Mater. Interfaces *12*, 13029-13039.
33. Lill, A.T., Cao, D.X., Schrock, M., Vollbrecht, J., Huang, J., Nguyen-Dang, T., Brus, V.V., Yurash, B., Leifert, D., Bazan, G.C., and Nguyen, T.Q. (2020). Organic Electrochemical Transistors Based on the Conjugated Polyelectrolyte PCPDTBT-SO3K (CPE-K). Adv. Mater. *32*, 1908120.